

# Two-field inflation from one complex scalar with symmetry breaking

Yoshihiko Abe<sup>1\*</sup>, Toshimasa Ito<sup>2†</sup>, and Koichi Yoshioka<sup>2‡</sup>

<sup>1</sup>*Department of Physics, University of Wisconsin-Madison, Madison, WI 53706, USA*

<sup>2</sup>*Department of Physics, Kyoto University, Kyoto 606-8502, Japan*

## Abstract

We study two-field inflation derived from a single complex scalar with a nonzero vacuum expectation value. Inflation is characterized by two parameters, the vacuum expectation value and the mass parameter of the phase mode, which give rise to a variety of inflationary structures. We categorize the potential trajectories of the two inflaton fields and determine the parameter regions consistent with current observational data. Furthermore, we examine the reheating process through the inflaton decay to right-handed neutrinos and the subsequent lepton number generation within these parameter regions. Our finding suggests that the existence of multiple fields can significantly alter the possibilities for inflaton oscillations and reheating.

---

\*yabe3@wisc.edu

†toshimasa.i@gauge.scphys.kyoto-u.ac.jp

‡yoshioka@gauge.scphys.kyoto-u.ac.jp

# Contents

<b>1</b>	<b>Introduction</b>	<b>1</b>
<b>2</b>	<b>Motions of inflaton with symmetry breaking</b>	<b>2</b>
2.1	Complex scalar with non-minimal coupling . . . . .	2
2.2	Slow-roll and slow-turn approximation . . . . .	4
2.2.1	Equations of motion and inflation parameters . . . . .	4
2.2.2	Behavior of slow-roll parameters . . . . .	5
2.3	Slow roll versus slow turn . . . . .	7
2.4	Classification of inflation trajectory . . . . .	9
<b>3</b>	<b>Constraints from cosmological observations</b>	<b>10</b>
3.1	Transfer functions and observables . . . . .	11
3.2	Spectral index and running spectrum . . . . .	12
3.3	Constraints on potential parameters . . . . .	14
3.3.1	$\phi_* > v_\phi$ and $v_\phi \ll 1$ . . . . .	14
3.3.2	$\phi_* > v_\phi$ and $v_\phi = \mathcal{O}(10)$ . . . . .	17
3.3.3	$\phi_* < v_\phi$ and $v_\phi = \mathcal{O}(10)$ . . . . .	19
3.3.4	$\phi_* < v_\phi$ and $v_\phi = \mathcal{O}(1)$ . . . . .	21
<b>4</b>	<b>Cosmic reheating</b>	<b>23</b>
4.1	Coupling to RH neutrinos . . . . .	23
4.2	Reheating and leptogenesis . . . . .	24
<b>5</b>	<b>Conclusions</b>	<b>28</b>
<b>A</b>	<b>Scalar field dynamics</b>	<b>29</b>
A.1	EOMs . . . . .	29
A.2	Geometry of scalar fields . . . . .	30
<b>B</b>	<b>Slow-roll and slow-turn parameters</b>	<b>30</b>
<b>C</b>	<b>Formulae of cosmological observables</b>	<b>31</b>
C.1	Transfer functions . . . . .	31
C.2	Cosmological observables . . . . .	32

## 1 Introduction

Inflation in the early universe gives a natural solution to the horizon and the flatness problems of the big-bang theory, and generates the primordial perturbations [1–6]. The inflationary expansion driven by a single scalar field has been extensively studied. Further,

multiple fields inflation models have also been studied with field theoretical [7–16] and other motivations such as supergravity and string theory [17, 18].

We consider a two-field inflation model from a single complex scalar field with a non-minimal coupling to gravity, which is assumed to develop a non-vanishing vacuum expectation value (VEV). If we consider only one of the radial and phase (Nambu-Goldstone) components to play the role of the inflaton, the inflationary expansion is realized by the similar dynamics to the new inflation [3], the chaotic inflation [6], the natural inflation [19–24], the Higgs inflation [25–29], etc. The VEV and the soft-breaking mass parameter of the phase mode determine the preferred inflation scenario.

In this paper, we study the details of two-field inflation from a single complex scalar with symmetry breaking. The inflation trajectories are classified according to the field component that drives inflation, with the VEV and soft-breaking mass parameter being varied. Subsequently, we show the parameter space of our inflation model that is consistent with the current cosmological observations. The classification of trajectories enables us to comprehend the typical inflation features and predictions. It is found that the Higgs-like inflation driven by the radial mode is favored in the wide region, while various other types can realize the successful inflation. Furthermore, we investigate the possibility of reheating the universe through the decay to right-handed (RH) neutrinos from a complex inflaton field with the non-minimal coupling.

This paper is organized as follows. In Section 2, we introduce our model and classify the inflation trajectories into typical three categories. Section 3 shows the parameter space consistent with the experimental constraints from the current cosmological observations. In Section 4, we discuss the reheating via the inflaton decay to RH neutrinos and evaluate the reheating temperature consistent with the thermal leptogenesis. Section 5 is devoted to our conclusions. The details of the notation and definition of parameters are summarized in Appendices.

## 2 Motions of inflaton with symmetry breaking

We first introduce our two-field inflation model and analyze the inflation dynamics by solving the equations of motion (EOMs). In this paper, we set the reduced Planck scale  $M_P \approx 2.4 \times 10^{18}$  GeV to be unity otherwise stated. We use the Minkowski metric convention  $\eta_{\mu\nu} = \text{diag}(+1, -1, -1, -1)$ .

### 2.1 Complex scalar with non-minimal coupling

We consider a complex scalar field  $\Phi$  with a non-minimal coupling to gravity. In this paper, we start our discussion from the following action:

$$S = \int d^4x \sqrt{-g_J} \left[ -\frac{1}{2} \Omega^2(\Phi) R_J + g_J^{\mu\nu} \partial_\mu \Phi \partial_\nu \Phi^* - U(\Phi, \Phi^*) \right], \quad (2.1)$$

where we introduce the non-minimal coupling  $\xi$ ,

$$\Omega^2(\Phi) = 1 + 2\xi|\Phi|^2. \quad (2.2)$$

$R_J$  is the Ricci scalar obtained from the Jordan frame metric  $g_{J\mu\nu}$ . Let the potential  $U(\Phi, \Phi^*)$  be given by

$$U(\Phi, \Phi^*) = \frac{\lambda}{2}|\Phi|^4 - \frac{\mu_\Phi^2}{2}|\Phi|^2 - \frac{m_\chi^2}{4}(\Phi^2 + \Phi^{*2}) + U_0, \quad (2.3)$$

as considered in Ref. [30] in the context of dark matter. The third term explicitly breaks the U(1) phase rotation symmetry of  $\Phi$  to  $\mathbb{Z}_2$  and generates the pseudo Nambu-Goldstone boson (pNGB) mass. The parameter  $m_\chi (\geq 0)$  is called as the soft-breaking mass. For a transformation  $\Phi \mapsto e^{i\pi/2}\Phi$ , the action is invariant under a sign flip of  $m_\chi^2$ ,  $m_\chi^2 \mapsto -m_\chi^2$ . That implies we can impose  $m_\chi^2 \geq 0$  consistently in the model. The ultraviolet completeness of this pNGB mass term is not specified in this paper, but its origin is discussed in several works [31–36].

We suppose that the scalar field  $\Phi$  develops a non-vanishing VEV  $v_\phi$ . The stationary condition allows us to derive the relations among  $\mu_\Phi^2$ ,  $U_0$ , and  $v_\phi$ , demanding that  $U = 0$  at the vacuum. If we parameterize  $\Phi$  in the non-linear representation as

$$\Phi = \frac{\phi}{\sqrt{2}}e^{i\chi}, \quad (2.4)$$

the scalar potential for the fields  $\phi$  and  $\chi$  is given by

$$U(\phi, \chi) = \frac{\lambda}{8}(\phi^2 - v_\phi^2)^2 + \frac{m_\chi^2}{4}\phi^2(1 - \cos 2\chi). \quad (2.5)$$

We note that  $\chi$  is a dimensionless variable.

In order to move to the Einstein frame from the Jordan frame [25, 28, 29, 37–40], we consider the field-dependent Weyl rescaling

$$g_{\mu\nu} = \Omega^2 g_{J\mu\nu} = (1 + \xi\phi^2)g_{J\mu\nu}, \quad (2.6)$$

where  $g_{\mu\nu}$  denotes the metric in the Einstein frame. This redefinition results in the following action

$$S = \int d^4x \sqrt{-g} \left[ -\frac{R}{2} + \frac{1 + \xi\phi^2 + 6\xi^2\phi^2}{2(1 + \xi\phi^2)^2} \partial_\mu \phi \partial^\mu \phi + \frac{\phi^2}{2(1 + \xi\phi^2)} \partial_\mu \chi \partial^\mu \chi - V(\phi, \chi) \right], \quad (2.7)$$

where  $R$  represents the Ricci scalar of  $g_{\mu\nu}$ , and the inflaton potential is given by

$$V(\phi, \chi) := \frac{U(\phi, \chi)}{(1 + \xi\phi^2)^2} = \frac{\lambda(\phi^2 - v_\phi^2)^2 + 2m_\chi^2\phi^2(1 - \cos 2\chi)}{8(1 + \xi\phi^2)^2}. \quad (2.8)$$

In the following, we refer to the first term in (2.8) as the Higgs potential and the second term as the pNGB potential, respectively. Note that the pNGB potential differs from the usual natural inflation potential in Refs. [19–24] in that the overall coefficient of the potential depends on  $\phi$ , which naturally arises from the pNGB soft-breaking term in our case.

The field space metric  $K_{ab}(\varphi)$  for real scalar fields  $\varphi$  is generally defined by the kinetic term as

$$\mathbf{L}_{\text{kin.}} = \frac{1}{2} K_{ab}(\varphi) \partial_\mu \varphi^a \partial_\nu \varphi^b g^{\mu\nu}, \quad (2.9)$$

where  $\varphi$  is the multiplet of scalar fields and indices  $a$  and  $b$  run all components. In the present model,  $\varphi^1 = \phi$  and  $\varphi^2 = \chi$ , and their metric reads from (2.7) as

$$K_{ab} = \text{diag} \left( \frac{1 + \xi\phi^2 + 6\xi^2\phi^2}{(1 + \xi\phi^2)^2}, \frac{\phi^2}{1 + \xi\phi^2} \right). \quad (2.10)$$

## 2.2 Slow-roll and slow-turn approximation

### 2.2.1 Equations of motion and inflation parameters

The equations of motion for the background fields are given by

$$\frac{d^2\phi}{dN^2} + \gamma_{11}^1 \left( \frac{d\phi}{dN} \right)^2 + \gamma_{22}^1 \left( \frac{d\chi}{dN} \right)^2 + (3 - \varepsilon) \left( \frac{d\phi}{dN} + K^{11} \frac{\partial}{\partial\phi} \ln V \right) = 0, \quad (2.11)$$

$$\frac{d^2\chi}{dN^2} + 2\gamma_{12}^2 \frac{d\phi}{dN} \frac{d\chi}{dN} + (3 - \varepsilon) \left( \frac{d\chi}{dN} + K^{22} \frac{\partial}{\partial\chi} \ln V \right) = 0, \quad (2.12)$$

where the e-folding  $N$  is defined by  $dN = H dt$  with  $H$  being the Hubble parameter, and  $\gamma_{bc}^a$  is the Levi-Civita connection derived from the field space metric  $K_{ab}$ . The slow-roll (SR) parameter  $\varepsilon$  is defined by

$$\varepsilon := -\frac{\dot{H}}{H^2} = \frac{1}{2} K_{11} \left( \frac{d\phi}{dN} \right)^2 + \frac{1}{2} K_{22} \left( \frac{d\chi}{dN} \right)^2. \quad (2.13)$$

For the detail, see Appendix A. In order to realize the SR inflation, the first SR condition

$$\varepsilon \ll 1, \quad (2.14)$$

is imposed [41–48]. This condition also appears in the case of single-field inflation.

The acceleration of the inflaton is characterized by the parameters

$$\eta^1 = \frac{d^2\phi}{dN^2} + \gamma_{11}^1 \left( \frac{d\phi}{dN} \right)^2 + \gamma_{22}^1 \left( \frac{d\chi}{dN} \right)^2, \quad (2.15)$$

$$\eta^2 = \frac{d^2\chi}{dN^2} + 2\gamma_{12}^2 \frac{d\phi}{dN} \frac{d\chi}{dN}, \quad (2.16)$$

in the  $\phi$ - and  $\chi$ -directions, respectively. As there are two fields, it is beneficial to decompose them into the direction of the inflation trajectory and the direction of rotation [42, 43, 49]. The former is called as the parallel direction and its unit vector is  $\hat{e}_\parallel$ . The latter is the vertical direction to  $\hat{e}_\parallel$  and its unit vector is  $\hat{e}_\perp$ . Using these unit vectors, the conditions of the acceleration for successful inflation are given by

$$\left| \frac{\eta_\parallel}{v} \right| := \left| \frac{K_{ab} \hat{e}_\parallel^a \eta^b}{v} \right| \ll 1, \quad (2.17)$$

$$\frac{\eta_\perp}{v} := \frac{K_{ab} \hat{e}_\perp^a \eta^b}{v} \ll 1, \quad (2.18)$$

where  $v = \sqrt{2\varepsilon}$  is the speed of field vector [41–43, 46]. Eq. (2.17) is the second SR condition and Eq. (2.18) is called the slow-turn (ST) condition. The ST condition is one of the indication of small vertical acceleration. Once the SR conditions (2.14), (2.17) and the ST condition (2.18) are satisfied, the SR and ST parameters are well approximately expressed with the inflaton potential  $V$  [46],

$$\varepsilon \approx \frac{1}{2} K^{ab} \partial_a \ln V \partial_b \ln V, \quad (2.19)$$

$$\frac{\eta_\parallel}{v} \approx -\hat{e}_\parallel^a (\partial_a \partial_b \ln V - \gamma_{ab}^c \partial_c \ln V) \hat{e}_\parallel^b, \quad (2.20)$$

$$\frac{\eta_\perp}{v} \approx -\hat{e}_\parallel^a (\partial_a \partial_b \ln V - \gamma_{ab}^c \partial_c \ln V) \hat{e}_\perp^b. \quad (2.21)$$

The unit vector in the parallel and vertical directions are expressed as

$$\hat{e}_\parallel^a = \frac{1}{v} \frac{d\varphi^a}{dN} \approx \frac{-K^{ab} \partial_b \ln V}{\sqrt{K^{cd} \partial_c \ln V \partial_d \ln V}}, \quad (2.22)$$

$$\hat{e}_\perp^a \approx \frac{\pm (K^{ab} - \hat{e}_\parallel^a \hat{e}_\parallel^b) (\partial_b \partial_c \ln V - \gamma_{bc}^d \partial_d \ln V) \hat{e}_\parallel^c}{\sqrt{(K^{ab} - \hat{e}_\parallel^a \hat{e}_\parallel^b) (\partial_a \partial_c \ln V - \gamma_{ac}^e \partial_e \ln V) (\partial_b \partial_d \ln V - \gamma_{bd}^f \partial_f \ln V) \hat{e}_\parallel^c \hat{e}_\parallel^d}}. \quad (2.23)$$

The direction of  $\hat{e}_\perp$  is chosen so that  $\eta_\perp \geq 0$ . We can use the EOMs to show that the above expression of the vertical unit vector is equivalent to  $K^{ab} J_{bc} \hat{e}_\parallel^c$  with some asymmetric  $J_{ab}$ , which is another expression according to the definition of perpendicular to  $\hat{e}_\parallel$ . In the case of two-dimensional field space, a simple solution is  $J_{ab} = \sqrt{\det K} / v \epsilon_{ab}$ , where  $\epsilon_{ab}$  is the totally asymmetric tensor. Note that all of the above quantities are written in terms of fields and their derivatives through the potential  $V$  and the field space metric  $K_{ab}$ , which values are obtained by solving the equations of motion (2.11) and (2.12).

### 2.2.2 Behavior of slow-roll parameters

We start our discussion from the parameter dependence of the SR parameters  $\varepsilon$  and  $|\eta_\parallel/v|$ . Figure 1 shows the dependence of the soft-breaking mass  $m_\chi$  and the field value  $\phi$ . In the left panels, the  $m_\chi$  dependence is given with  $\lambda = 1$ ,  $v_\phi = 10^{-4}$ ,  $\phi = 1$ , and  $\chi = \frac{\pi}{3}$ . The blue, orange, and green lines represent the results obtained for  $\xi = 10$ ,  $10^3$ , and  $10^5$ ,

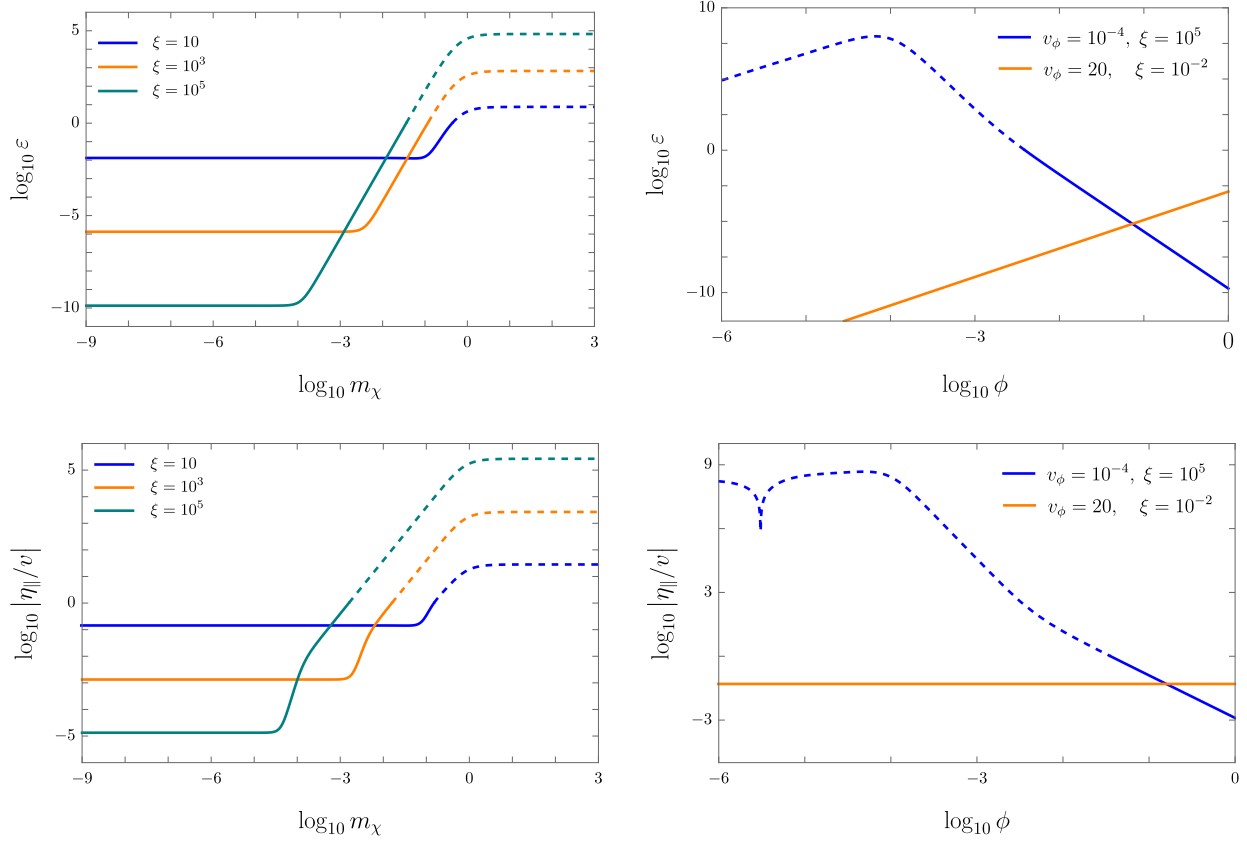


Figure 1: The  $m_\chi$  and  $\phi$  dependence of the slow-roll parameters. In the left panels, we set  $\lambda = 1$ ,  $v_\phi = 10^{-4}$ ,  $\phi = 1$ , and  $\chi = \frac{\pi}{3}$ . In the right panels,  $\lambda = 1$ ,  $m_\chi = 10^{-4}$ ,  $\chi = \pi/3$  and  $\xi = 10^5$  ( $\xi = 10^{-2}$ ) are used for  $v_\phi = 10^{-4}$  ( $v_\phi = 20$ ). The dashed lines indicate that the SR conditions are not satisfied.

respectively. The value of VEV  $v_\phi$  is motivated from the energy scale of grand unification or lepton number violation. When  $m_\chi$  is sufficiently smaller than the Planck scale, the inflation is primarily driven by  $\phi$  and effectively reduces to the single-field inflation, analogous to the Higgs inflation. In this case, the SR parameters are approximately given by

$$\varepsilon \approx \frac{8(1 + \xi v_\phi^2)^2 \phi^2}{(\phi^2 - v_\phi^2)^2 (1 + \xi \phi^2 + 6\xi^2 \phi^2)}, \quad (2.24)$$

$$\frac{\eta_{\parallel}}{v} \approx \frac{4(1 + \xi v_\phi^2)(1 + \xi \phi^2)[v_\phi^2 + \phi^2(1 + 2\xi \phi^2 + 12\xi^2 \phi^2)]}{(\phi^2 - v_\phi^2)^2 (1 + \xi \phi^2 + 6\xi^2 \phi^2)^2}. \quad (2.25)$$

These expressions do not involve the soft-breaking mass. When  $m_\chi$  is sufficiently large, the pNGB potential tends to dominate the inflation. Consequently, the SR parameters do not involve  $m_\chi$  again since  $m_\chi$  becomes an overall parameter of the inflaton potential. We note that a larger  $\xi$  makes the inflaton potential flatter, which results in smaller SR parameters. For the detail expressions of the SR parameters, see Appendix B.

The right panels of Figure 1 show the  $\phi$  dependence of SR parameters with  $\lambda = 1$ ,  $m_\chi = 10^{-4}$ ,  $\chi = \pi/3$  and  $\xi = 10^5$  ( $\xi = 10^{-2}$ ) for  $v_\phi = 10^{-4}$  ( $v_\phi = 20$ ). This large VEV is motivated by the fact that the natural inflation requires VEV beyond the Planck scale [21]. A large value of  $\phi$  ( $> v_\phi$ ) results in a reduction of the SR parameters due to the proportionality  $\varepsilon \propto \phi^{-4}$  and  $\eta_{\parallel}/v \propto \phi^{-2}$ , as derived from the approximate formulae presented in Appendix B. These behaviors can be attributed to the dominance of the Higgs potential in the large  $\phi$  region. In contrast, for a small value of  $\phi$  ( $< v_\phi$ ), the SR parameters are expressed as

$$\varepsilon \approx \frac{8\phi^2}{\lambda^2 v_\phi^8} (A^2 + m_\chi^4 \sin^2 2\chi), \quad (2.26)$$

$$\frac{\eta_{\parallel}}{v} \approx \frac{4}{\lambda v_\phi^4} \frac{A^3 + 3Am_\chi^4 \sin^2 2\chi - 2m_\chi^6 \cos 2\chi \sin^2 2\chi}{A^2 + m_\chi^4 \sin^2 2\chi}, \quad (2.27)$$

where  $A = \lambda v_\phi^2(1 + \xi v_\phi^2) - 2m_\chi^2 \sin^2 \chi$ . It is found that  $\varepsilon$  becomes small and  $|\eta_{\parallel}/v|$  is constant for sufficiently small  $\phi$  due to the flatness of the inflaton potential. When  $m_\chi \ll \sqrt{\lambda} v_\phi$  and  $\xi v_\phi^2 \ll 1$ , we have

$$\left| \frac{\eta_{\parallel}}{v} \right| \approx \frac{4}{v_\phi^2}, \quad (2.28)$$

which implies that the VEV must exceed the Planck scale in order to achieve a SR inflation with the Higgs potential in the region of small field value  $\phi$ .

### 2.3 Slow roll versus slow turn

Let us consider the condition characterizing the two-field nature of the inflationary trajectory according to Eqs. (2.11) and (2.12). Because the turn in the field space can be dominant if  $|\eta_{\parallel}/v| \ll \eta_{\perp}/v$  [46], let us define

$$\mu := \max\left(\frac{\eta_{\perp}/v}{|\eta_{\parallel}/v|}\right), \quad (2.29)$$

which is evaluated on the inflationary trajectory. This  $\mu$  parameter represents how much the two-field nature originating from the movements of  $\phi$  and  $\chi$  is strong.

We use  $\phi_*$  and  $\chi_*$  for the horizon-exit values of these fields. As typical values of  $\chi_*$ , we choose  $\chi_* = 23\pi/48$ ,  $\pi/3$ , and  $\pi/100$ , which respectively correspond to the following three cases:

- (a) Near the top of the pNGB potential
- (b) Middle of the pNGB potential
- (c) Near the bottom of the pNGB potential

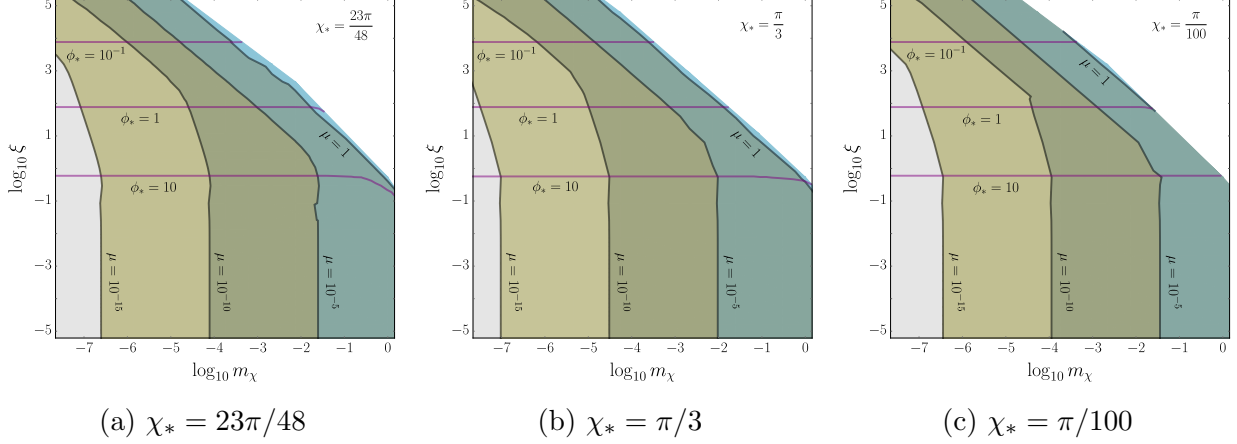


Figure 2: The contours of the  $\mu$  parameter (2.29) in the  $(m_\chi, \xi)$  plane. We set  $\lambda = 1$  and  $\phi_* > v_\phi = 10^{-4}$ . Each horizontal purple line means  $\phi_*$  takes a fixed value explicitly stated along each line. These plots are evaluated with  $N$  being fixed at 55. In the right-upper white region, either SR or ST condition is violated until reaching  $N = 55$ .

Figure 2 shows the  $\mu$  parameter in the  $(m_\chi, \xi)$  plane for the aforementioned values of  $\chi_*$ . We set  $\lambda = 1$  and  $\phi_* > v_\phi = 10^{-4}$  as in Section 2.2.2, and evaluate  $\mu$  at the e-folding  $N = 55$ .

For large  $m_\chi$  or  $\xi$ , it is not possible to satisfy the SR and/or ST conditions for a fixed e-folding, as shown by the white region in Figure 2. In the figure,  $\phi$  tends to drive the inflation with the field-turning effect becoming dominant when the pNGB potential is effective as  $m_\chi$  increases. This implies the SR/ST violating (white) region for large  $m_\chi$  with a fixed  $\xi$ . Conversely, a larger  $\xi$  makes  $\phi_*$  smaller in the  $\phi_* > v_\phi$  region due to the flattening effect of the inflaton potential. For too large  $\xi$ , the inflaton potential for  $\phi$  becomes too flat, which may result in a too-slow acceleration. That implies a large  $\xi$  results in large  $\mu$  for a fixed  $m_\chi$  (a fixed size of the pNGB potential).

If  $m_\chi$  or  $\xi$  is relatively large, the inflaton tends to move in the  $\chi$ -direction. It can be seen from the ratio of the gradient of the inflaton potential

$$\frac{K^{22}\partial_2 \ln V}{K^{11}\partial_1 \ln V} = \frac{m_\chi^2(1 + \xi\phi^2 + 6\xi^2\phi^2) \sin 2\chi}{\phi[\lambda\phi^2 + 2m_\chi^2(1 - \xi\phi^2) \sin^2 \chi]}, \quad (2.30)$$

which is proportional to  $m_\chi^2$  and  $\xi^2$  when the dynamics of  $\phi$  is dominated by the Higgs potential. We also find a simple approximated formula for the  $\mu$  parameter for small  $v_\phi$  and  $m_\chi$

$$\mu \approx \frac{m_\chi^2 \xi^{\frac{5}{2}} v_\phi^2 \sin(2\chi_*)}{8\lambda}. \quad (2.31)$$

It is found from this expression that  $\mu$  is vanishing for  $m_\chi = 0$ , and is positively proportional to  $\xi$  as  $\mu \propto m_\chi^2 \xi^{5/2}$ . From these behaviors, we find that a large  $\mu$  can be realized in the large  $m_\chi$  and large  $\xi$  region, which implies the strong nature of two-field inflation.

It is noted that the inflaton potential (2.8) is rewritten as

$$V(\phi, \chi) = \lambda \frac{(\phi^2 - v_\phi^2)^2 + 2\left(\frac{m_\chi}{\sqrt{\lambda}}\right)^2 \phi^2 (1 - \cos 2\chi)}{8(1 + \xi\phi^2)^2}. \quad (2.32)$$

While we have shown Figure 2 with a fixed value  $\lambda = 1$ , the  $\mu$  parameter for other values of  $\lambda$  can be obtained by rescaling  $m_\chi$  as  $m_\chi/\sqrt{\lambda}$ , since  $\mu$  is roughly given by the ratio of the potential and the overall  $\lambda$  dependence is cancelled, as seen from the above potential.

## 2.4 Classification of inflation trajectory

The parameter  $\mu$  defined in Eq. (2.29) is an appropriate quantity for characterizing the multi-field nature of the inflaton motion. In this section, we classify the inflation trajectory with the help of  $\mu$ . This classification enables us to comprehend the multi-field nature of inflation without having to examine in great detail the complex motions of inflatons due to their interactions with each other.

Figure 3 shows typical inflation trajectories in the present two-field model. The vectors in the figures indicate the potential gradients appearing in the EOMs,  $K^{ab}\partial_b \ln V$  with  $a, b = 1, 2$ . The red and blue solid lines represent the trajectories with  $N = 50$  and  $N = 60$ , respectively. In the shaded region, the SR and/or ST condition is not satisfied. We here adopt the values of  $v_\phi = 10^{-4}$  and  $v_\phi = 20$  as in the previous case. In the upper (lower) three panels, the VEV of  $\Phi$  is chosen as  $v_\phi = 10^{-4}$  ( $v_\phi = 20$ ), which is the large (small) VEV case under the situation  $\phi_* > v_\phi$  ( $\phi_* < v_\phi$ ).

When  $m_\chi$  is small and the pNGB potential contribution is irrelevant (the left panels of Figure 3), the inflation is mainly driven by  $\phi$ . This is similar to the single-field inflation scenario such as the Higgs inflation and chaotic inflation. In this case,  $\mu \ll 1$  as a result of little motion in the  $\chi$ -direction during the inflation. As  $m_\chi$  increases,  $\chi$  also plays a part of the inflaton as well as  $\phi$ , which is shown in the middle panels of Figure 3. As illustrated in the figures, the multi-field effect becomes pronounced, frequently resulting in  $\mu \gtrsim 1$ . In the right panels, where  $m_\chi$  is large, the inflaton trajectory is mainly along the pNGB  $\chi$ -direction, similar to the natural inflation. In this case, the inflation process is also driven by a single field, which results in the situation of  $\mu \ll 1$ .

Let us classify the inflaton trajectories into the following three categories in the present two-field inflation model:

- Higgs inflation type driven by  $\phi$  (shown by (a) and (d))
- Mixed type with both  $\phi$  and  $\chi$  as inflaton (shown by (b) and (e))
- Natural inflation type mainly driven by  $\chi$  (shown by (c) and (f))

In the following section, we examine the relation between inflationary trajectories and the cosmological observables. The symbols H(iggs), M(ixed), and N(atural) will be used to indicate which of these types the inflation trajectory we are referring to.

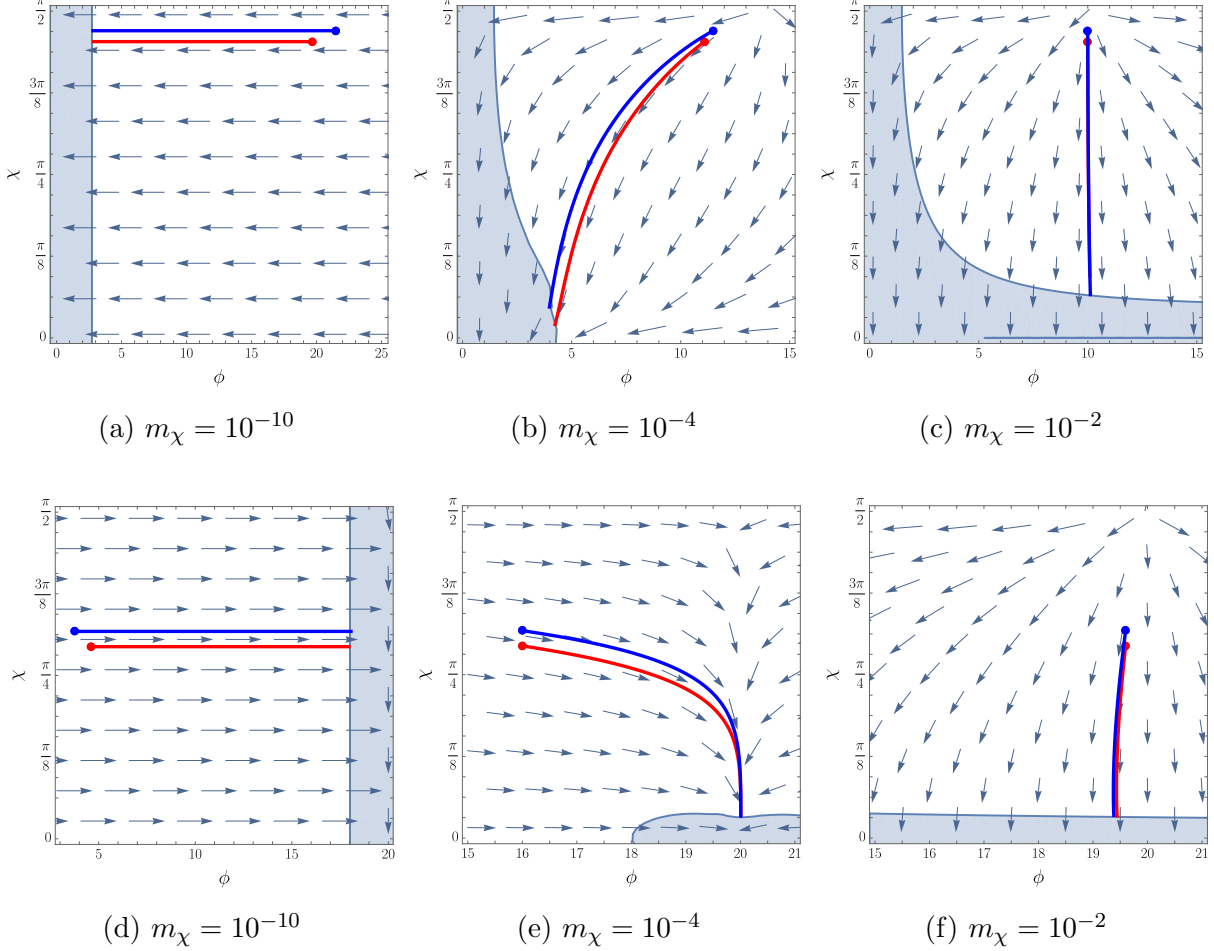


Figure 3: Typical inflation trajectories in the present two-field model. The red and blue lines represent the trajectories with  $N = 50$  and  $N = 60$ , respectively. The red and blue circle represent the initial value of the inflaton with  $N = 50$  and  $N = 60$ , respectively. The arrows indicate the potential gradients  $K^{ab}\partial_b \ln V$ , which corresponds to the field velocity in the slow-roll and slow-turn limits. The SR and/or ST condition is not satisfied in the shaded region. The parameters are chosen as follows: (Upper panels)  $\lambda = 10^{-10}$ ,  $v_\phi = 10^{-4}$ ,  $\xi = 10^{-2}$ ,  $\chi_* = 34\pi/75$  ( $N = 50$ ), and  $\chi_* = 47\pi/100$  ( $N = 60$ ). (Lower panels)  $\lambda = 1$ ,  $v_\phi = 20$ ,  $\xi = 10^{-2.6}$ ,  $\chi_* = 5\pi/17$  ( $N = 50$ ), and  $\chi_* = 20\pi/63$  ( $N = 60$ ).

### 3 Constraints from cosmological observations

This section presents an analysis of the inflation observables and the parameter constraints for the current two-field inflation model.

### 3.1 Transfer functions and observables

In the context of single-field inflation, the observables are derived from the fluctuations of the inflaton field and the curvature perturbation, denoted by  $\mathcal{R}$ , in the co-moving gauge on hypersurfaces at a constant time [50–53]. In the case of multi-field inflation, this scalar fluctuation is defined as a projection of the multi-field fluctuations onto the tangent direction of the inflation trajectory:

$$\mathcal{R} = \frac{K_{ab}\hat{e}_{\parallel}^a\delta\varphi_f^b}{v}. \quad (3.1)$$

The perturbation  $\delta\varphi_f$  is the multi-field version of the Mukhanov-Sasaki variable [46, 53, 54]

$$\delta\varphi_f = \delta\varphi + \psi\frac{d\varphi}{dN}, \quad (3.2)$$

where  $\delta\varphi$  is the scalar field fluctuation and  $\psi$  is a part of the diagonal metric perturbation [50, 51, 54]. Furthermore, it is necessary to consider the fluctuations in the vertical direction with respect to the inflation trajectory, which give rise to the isocurvature perturbation [46, 55]

$$\mathcal{S} = \frac{K_{ab}\hat{e}_{\perp}^a\delta\varphi_f^b}{v}. \quad (3.3)$$

These two perturbations  $\mathcal{R}$  and  $\mathcal{S}$  have the following relation [46, 55–57]

$$\begin{pmatrix} \mathcal{R} \\ \mathcal{S} \end{pmatrix} = \begin{pmatrix} 1 & T_{\mathcal{R}\mathcal{S}} \\ 0 & T_{\mathcal{S}\mathcal{S}} \end{pmatrix} \begin{pmatrix} \mathcal{R}_* \\ \mathcal{S}_* \end{pmatrix}. \quad (3.4)$$

The values at the horizon exit are denoted with  $*$  such as  $\mathcal{R}_*$  and  $\mathcal{S}_*$ . This relation indicates that the curvature perturbation  $\mathcal{R}$  is not frozen after the horizon exit and the isocurvature perturbation  $\mathcal{S}$  contributes to it through the transfer function  $T_{\mathcal{R}\mathcal{S}}$  [27, 42, 43, 52, 57, 58].

In contrast to the single-field inflation scenario,  $T_{\mathcal{R}\mathcal{S}}$  can contribute to the inflationary observables in the multi-field case. The power spectrum  $\mathcal{P}_{\mathcal{R}}$  and tensor-to-scalar ratio  $r$  are given by [41, 46]

$$\mathcal{P}_{\mathcal{R}} = \frac{V_*}{24\pi^2\epsilon_*}(1 + T_{\mathcal{R}\mathcal{S}}^2), \quad r = \frac{16\epsilon_*}{1 + T_{\mathcal{R}\mathcal{S}}^2}. \quad (3.5)$$

In addition, we consider the spectral index  $n_s$  and the running spectrum  $\alpha$  given by

$$n_s = 1 + \frac{d\ln\mathcal{P}_{\mathcal{R}}}{d\ln k}, \quad \alpha = \frac{dn_s}{d\ln k}, \quad (3.6)$$

and the isocurvature fraction [27, 57, 59, 60]

$$\beta_{\text{iso}} = \frac{T_{\mathcal{S}\mathcal{S}}^2}{1 + T_{\mathcal{R}\mathcal{S}}^2 + T_{\mathcal{S}\mathcal{S}}^2}. \quad (3.7)$$

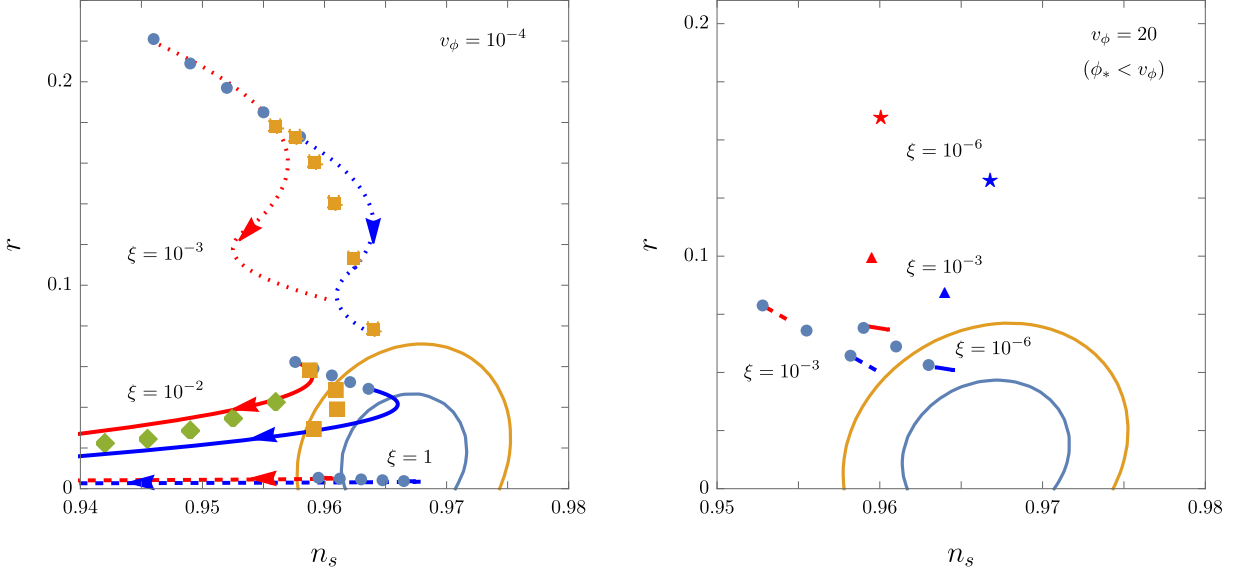


Figure 4: Typical predictions for the spectral index and the tensor-to-scalar ratio for a fixed initial value  $\chi_* = \pi/3$ . The red and blue lines correspond to  $N = 50$  and  $N = 60$ . The dashed, solid and dotted lines in the left panel correspond to  $\xi = 1$ ,  $10^{-2}$ , and  $10^{-3}$ , respectively. The dashed (solid) lines in the right panel are for  $\xi = 10^{-3}$  ( $\xi = 10^{-6}$ ). The soft-breaking mass takes  $0 \leq m_\chi \leq 1.4 \times 10^{-5}$  ( $\xi = 10^{-3}$ ),  $0 \leq m_\chi \leq 2.3 \times 10^{-5}$  ( $\xi = 10^{-2}$ ) and  $0 \leq m_\chi \leq 1.1 \times 10^{-4}$  ( $\xi = 1$ ) in the left panel, and  $0 \leq m_\chi \leq 7.0 \times 10^{-6}$  in the right panel. The arrows on the lines indicate the direction  $m_\chi$  increases. The marks mean the fixed  $m_\chi$  behaviors:  $m_\chi = 0$  (circle),  $6 \times 10^{-6}$  (square),  $7.6 \times 10^{-6}$  (diamond),  $5.9 \times 10^{-6}$  (blue star),  $7.0 \times 10^{-6}$  (red star),  $6.2 \times 10^{-6}$  (blue triangle), and  $7.0 \times 10^{-6}$  (red triangle). The contours are the experimental bounds with  $1\sigma$  and  $2\sigma$  confidence levels by the Planck observation.

These quantities also depend on the transfer functions [27, 46, 57, 61], and all of these can be expressed by the parameters and field values in the present inflation model. See Appendix C for the detail.

These inflationary observables are experimentally constrained by the Planck Collaboration [62]

$$\begin{aligned} \mathcal{P}_{\mathcal{R}} &= (2.1 \pm 0.1) \times 10^{-9}, & r &< 0.07, & n_s &= 0.9649 \pm 0.0042, \\ \alpha &= -0.0045 \pm 0.0067, & \beta_{\text{iso}} &< 0.038. \end{aligned} \quad (3.8)$$

### 3.2 Spectral index and running spectrum

Figure 4 shows typical predictions in the  $(n_s, r)$  plane in the present two-field model. The power spectrum is normalized by  $\lambda$  as  $\mathcal{P}_{\mathcal{R}} = 2.1 \times 10^{-9}$  such that it is consistent with

the Planck observation. The parameters  $v_\phi$  and  $\chi_*$  are fixed at specific values. In the left panel, we explicitly use  $v_\phi = 10^{-4}$  and  $\chi_* = \pi/3$ , on the other hand  $v_\phi = 20$ ,  $\chi_* = \pi/3$  in the right panel. In addition to these, we explicitly use  $0 \leq m_\chi \leq 1.4 \times 10^{-5}$  ( $\xi = 10^{-3}$ ),  $0 \leq m_\chi \leq 2.3 \times 10^{-5}$  ( $\xi = 10^{-2}$ ) and  $0 \leq m_\chi \leq 1.1 \times 10^{-4}$  ( $\xi = 1$ ) in the left panel and  $0 \leq m_\chi \leq 7.0 \times 10^{-6}$  ( $\xi = 10^{-6}$  and  $\xi = 10^{-3}$ ) in the right panel.

We first focus on the left panel of Figure 4. When  $m_\chi$  is sufficiently small, the Higgs potential dominates the inflaton potential. Consequently, the prediction of the observables is similar to the Higgs inflation case. In this cases,  $n_s(r)$  becomes large (small) as  $N$  increases. This is due to the fact that the initial value  $\phi_*$  must be sufficiently large in order to flatten the inflaton potential during the inflation, which results in larger  $n_s$  and small  $r$ . The change in  $n_s$  occurs more quickly when  $N$  is larger, which makes  $\phi_*$  larger, since  $m_\chi$  appears in the Lagrangian in the combination of  $m_\chi^2 \phi^2$ . As  $m_\chi$  increases, the inflaton motion in the  $\chi$ -direction also contributes to the inflation. Consequently,  $\phi_*$  becomes more closely at the bottom of the Higgs potential in order to achieve a specific fixed e-folding. This results in a smaller inflaton potential, which in turn implies smaller  $\varepsilon_*$  due to the Planck normalization. From the single-field inflation analogy, this gives rise to an increase in the value of  $n_s$ . From this consideration, we can argue that the value of  $n_s$  increases when the pNGB mode also contributes to the inflation, provided that  $\phi_* > v_\phi$ . Conversely, sufficiently large  $m_\chi$  can drive the natural-like inflation. The left panel of Figure 4 shows that larger  $m_\chi$  results in a reduction in both  $n_s$  and  $r$ . This feature is also seen in the context of natural inflation. For small  $\xi$  and large  $m_\chi$ , the pNGB part of the action (2.7) during the inflation is approximated as

$$S \approx \int d^4x \sqrt{-g} \left[ \frac{\phi_*^2}{2} \partial_\mu \chi \partial^\mu \chi - \frac{m_\chi^2 \phi_*^2}{4} (1 - \cos 2\chi) \right]. \quad (3.9)$$

This action shows that  $\phi_*$  being larger than Planck scale facilitates the flatter pNGB potential for the natural-like inflation. Consequently, we can conclude that the natural-like inflation is feasible despite  $v_\phi$  being smaller than the Planck scale. We note that a larger  $\xi$  flattens the inflaton potential enough and tends to result in a smaller value of  $r$ .

Let us move to the right panel of Figure 4. When  $m_\chi$  is sufficiently small, we can say that an increase of  $N$  results in an increase of  $n_s$  and a decrease of  $r$ . This is due to the fact that, in order to ensure the flatness of the inflaton potential during inflation, it is necessary for a larger value of  $N$  to initiate the inflation from the part of flatter potential. In this region, the inflation driven by almost only the radial component  $\phi$ . On the other hand, if the Higgs potential is no longer dominant, the natural inflation occurs with a particular  $m_\chi$ , which leads to a large  $r$ . This behavior can be seen in the figure, and we can say that natural-like inflation also occurs for a large VEV as the single-field natural inflation. Finally, we discuss the relation between  $\xi$  and the observables. When  $m_\chi$  is sufficiently small, the Higgs potential is dominant, so a larger  $\xi$  tilts the inflaton potential in the region of  $\phi < v_\phi$ . This results in smaller  $n_s$  and larger  $r$ . Conversely, if the pNGB potential is the dominant

one, a larger  $\xi$  leads to a flatter inflaton potential, which in turn results in a smaller  $r$ . These can be read from the right panel of Figure 4.

### 3.3 Constraints on potential parameters

We show the parameter space in the  $(m_\chi, \xi)$  plane which is consistent with the cosmological observations by considering three typical initial values  $\chi_*$ , as discussed in Section 2.3:

$$\chi_* = \frac{23\pi}{48}, \frac{\pi}{3}, \frac{\pi}{100}. \quad (3.10)$$

The discussion is mainly divided into the cases of  $\phi_* > v_\phi$  and  $\phi_* < v_\phi$ . These cases typically correspond to the large and small field inflation scenarios along with  $\phi$ , respectively. We investigate the inflationary features using  $v_\phi = 10^{-4}$  as the case of small VEV ( $\ll 1$ ) and  $v_\phi = 20$  as the case of large VEV ( $\sim \mathcal{O}(10)$ ). In addition to them, we also investigate the third case with  $v_\phi = 5$  as a typical intermediate VEV scale ( $\sim \mathcal{O}(1)$ ). In the following, we consider the four patterns of VEV and the  $\phi$  direction:

- (i)  $\phi_* > v_\phi = 10^{-4} \ll 1$
- (ii)  $\phi_* > v_\phi = 20 = \mathcal{O}(10)$
- (iii)  $\phi_* < v_\phi = 20 = \mathcal{O}(10)$
- (iv)  $\phi_* < v_\phi = 5 = \mathcal{O}(1)$

In each pattern, we analyze the inflation with various values of the soft-breaking mass  $m_\chi$ .

The inflaton trajectories are classified into three types, as discussed in Section 2.4 and referred to by the symbols H, M and N. In all figures of parameter constraints given below, the Planck normalization  $\mathcal{P}_R = 2.1 \times 10^{-9}$  is imposed to determine the coupling constant  $\lambda$ .

#### 3.3.1 $\phi_* > v_\phi$ and $v_\phi \ll 1$

First, we examine the case where the VEV is small and  $\phi$  is rolling down from a large initial value. Figure 5 shows the parameter space which is consistent with the observations, where we set  $v_\phi = 10^{-4}$ ,  $\phi_* > v_\phi$ , and  $N = 55$ . In the white region, the condition  $N = 55$  is not satisfied, which is found in the large  $m_\chi$  region. This is due to the fact that the Planck normalization provides an upper limit for  $m_\chi \phi_*$ , and the SR and ST conditions exclude small  $\phi_*$  for enough e-folding. The pink region is consistent with the observations and  $N = 55$ . The gray, blue, red colored regions are excluded by the constraints from the observations on  $n_s$ ,  $r$ , and  $\alpha$ , respectively. The black (brown) dashed line represents  $\phi_* = 1$  ( $\lambda = 1$ ). The Planck normalization and the perturbativity of the quartic coupling  $\lambda$  provides the upper bound on the non-minimal coupling, which is given by  $\xi \lesssim 10^5$ , as discussed in Refs. [25, 26, 29]. The soft-breaking mass parameter  $m_\chi$  determines which contribution of potential is dominant, the Higgs potential or the pNGB potential. In the following, the parameter space is analyzed with paying attention to the value of  $m_\chi$ .

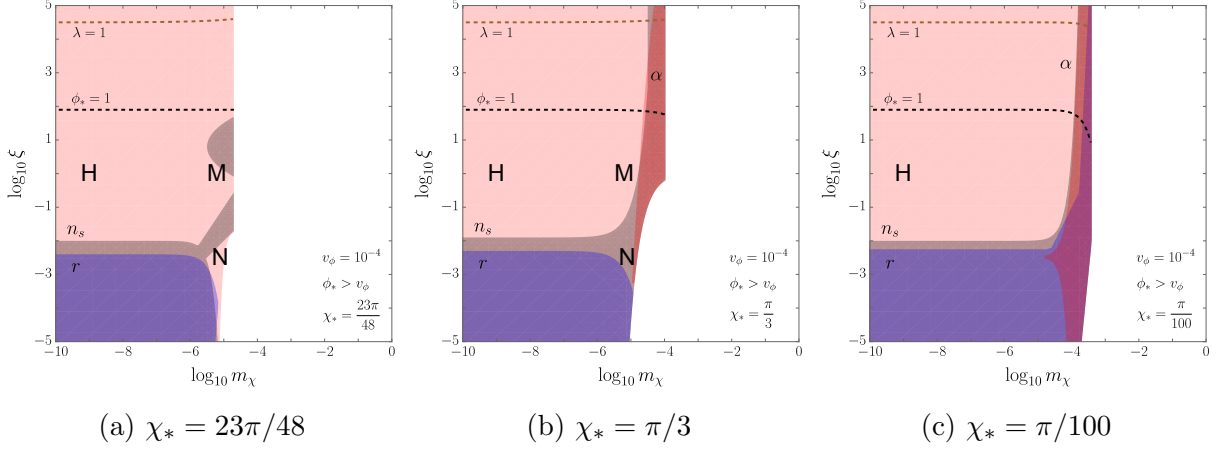


Figure 5: The allowed parameter region in the  $(m_\chi, \xi)$  plane for  $\phi_* > v_\phi = 10^{-4}$ . The pink region is consistent with the observations and  $N = 55$ . The gray, blue, and red colored regions are excluded by the constraint from the observations on  $n_s$ ,  $r$ , and  $\alpha$ , respectively.  $\phi_* = 1$  and  $\lambda = 1$  hold on the black and brown dashed lines, respectively.

We find some small allowed region labeled by N around  $(m_\chi, \xi) \sim (10^{-5}, 10^{-3})$  in Figure 5(a) where the inflation is mainly driven by  $\chi$ , and  $\phi$  oscillates at the end of inflation. It is noticed that the inflationary expansion in this region is similar to the one discussed in Refs. [12, 63].

**Small  $m_\chi$  region:** In the small  $m_\chi$  region, the inflation is dominantly driven by  $\phi$ , which region is labelled by H in the figure. There the spectral index and the tensor-to-scalar ratio are approximately given by

$$n_s \approx 1 - \frac{8(3 + 5\xi\phi_*^2 + 24\xi^2\phi_*^2 + 2\xi^2\phi_*^4 + 12\xi^3\phi_*^4)}{\phi_*^2(1 + \xi\phi_*^2 + 6\xi^2\phi_*^2)^2} + \mathcal{O}(m_\chi^2), \quad (3.11)$$

$$r \approx \frac{128}{\phi_*^2(1 + \xi\phi_*^2 + 6\xi^2\phi_*^2)} + \mathcal{O}(m_\chi^2), \quad (3.12)$$

where the e-folding is expressed as [64]

$$N \approx \frac{1 - \sqrt{1 + 32\xi + 192\xi^2} + 2(1 + 6\xi)\xi\phi_*^2 + 12\xi \ln \frac{1+12\xi+\sqrt{1+32\xi+192\xi^2}}{2(1+6\xi)(1+\xi\phi_*^2)}}{16\xi}. \quad (3.13)$$

When  $\xi$  is also small, these expressions reduce to

$$n_s \approx 1 - \frac{3}{N} + \mathcal{O}(m_\chi^2), \quad (3.14)$$

$$r \approx \frac{16}{N} + \mathcal{O}(m_\chi^2), \quad (3.15)$$

and are excluded by the observations as seen in Figure 5. This is due to the fact that a smaller  $\xi$  results in a more tilted inflaton potential, which makes the spacetime away from the de Sitter space and  $r$  becomes larger than the observed value. The above discussion and the approximate formulae lead to the conclusion that there is a lower bound for the non-minimal coupling  $\xi$ . This can be read from Figure 5 as  $\xi \gtrsim 10^{-2}$ , which is consistent with the result in Ref. [64].

Next, let us discuss the running spectrum. In the small  $\xi$  region, it is approximately given by

$$\alpha \approx -\frac{3}{N^2} + \mathcal{O}(m_\chi^2), \quad (3.16)$$

which implies that  $\alpha$  is consistent with the observation for sufficiently large e-folding  $N$  under the current situation. This result is to be expected since the magnitudes of  $|1 - n_s|$  and  $|\alpha|$  are generally hierarchical in single-field inflation [65]. On the other hand, for large  $\xi$ , we obtain the approximate formula for  $\alpha$ ,

$$\alpha \approx -\frac{32}{9\xi^2\phi_*^4}. \quad (3.17)$$

A large value of  $\xi$  ensures that  $\alpha$  remains sufficiently small and consistent with the experimental data. That means a hierarchy between  $|1 - n_s|$  and  $|\alpha|$ , and the inflation is mainly achieved by the Higgs potential part and reduces to the single-field inflation scenario effectively.

We also discuss the isocurvature fraction for small  $m_\chi$ . The general form is given by (3.7) and the transfer function  $T_{SS}$  is written as

$$T_{SS} = \exp \int_{N_*}^N \tilde{\beta} dN'. \quad (3.18)$$

The explicit form of the function  $\tilde{\beta}$  is found in Appendix C, which can be determined by the model parameters and field values obtained by solving the EOMs. In the present case,  $\tilde{\beta}$  is approximately given by

$$\tilde{\beta} \approx -\frac{8}{\phi^2} \quad (\xi \ll 1), \quad (3.19)$$

$$\tilde{\beta} \approx -\frac{4v_\phi^2}{3\phi^2} \quad (\xi \gg 1). \quad (3.20)$$

A negative, moderate  $\tilde{\beta}$  leads to an exponentially small  $T_{SS}$ , and thus  $\beta_{\text{iso}}$  is sufficiently small to be consistent with the observational data. Note here that the condition  $\xi \gg 1$  implies  $\phi_* \ll 1$ .

**Large  $m_\chi$  region:** If we have a large  $m_\chi$  and the  $\chi$  contribution, both  $\phi$  and  $\chi$  can play the roll of the inflaton when  $\xi$  is small, as shown in the left and middle panels of Figure 5. For the spectral index, we find that  $n_s$  becomes larger with increasing of  $m_\chi$  under  $\xi \ll 1$  as discussed in Figure 4, which leads to a contradiction to the observational data. Conversely, the parameter regions where the inflation is primarily driven by  $\chi$  can be allowed as shown in the left panel. In particular, the spectral index is approximated as

$$n_s \approx 1 - \frac{4(2 + T_{\mathcal{RS}}^2)}{(1 + T_{\mathcal{RS}}^2)\phi_*^2 \sin^2 \chi_*}, \quad (3.21)$$

when  $m_\chi \gg \sqrt{\lambda}v_\phi$  and  $\xi \ll 1$ . The spectral index on this inflation trajectory can match to the observations. That is driven by the pNGB mode with a help of the dynamical radial component. Furthermore, the inflation may also be allowed in the case of  $\xi \gg 1$ , where the pNGB mode contributes sufficiently, as shown in the left and middle panels of Figure 5. This is due to the fact that a large  $\xi$  not only flattens the inflaton potential but also facilitates the movement in the  $\chi$ -direction as discussed in Section 2.3. On the other hand, if the initial value  $\chi_*$  is sufficiently small as in the right panel, the inflaton moves almost no further in the  $\chi$ -direction, independently of  $v_\phi$ .

Finally, we give a comment on the isocurvature bound  $\beta_{\text{iso}}$ . The function  $\tilde{\beta}$  appearing in Eq. (3.18) is approximated as

$$\tilde{\beta} \approx -\frac{2}{\phi^2 \sin^2 \chi} \quad (\xi \ll 1), \quad (3.22)$$

$$\tilde{\beta} \approx -\frac{2\xi}{\sin^2 \chi} \quad (\xi \gg 1), \quad (3.23)$$

where we assume  $m_\chi \gg \sqrt{\lambda}v_\phi$  and  $v_\phi \ll 1$ . Since  $\tilde{\beta}$  is negative in the both cases, we can say that  $\beta_{\text{iso}}$  is sufficiently small in this case.

### 3.3.2 $\phi_* > v_\phi$ and $v_\phi = \mathcal{O}(10)$

We consider  $\phi_* > v_\phi$  with the VEV being a relatively large value of  $v_\phi = 20$ . Figure 6 shows the allowed parameter region for the inflation under this VEV and field value. The aforementioned colors are used to show the experimentally-excluded regions. In the white region, the e-folding  $N = 55$  cannot be satisfied with a large  $m_\chi$ , similar to Figure 5.

**Small  $m_\chi$  region:** In the small  $m_\chi$  region with  $\phi_* > v_\phi = 20$  and  $\xi \gg 1$ , the spectral index, the tensor-to-scalar ratio, and the running spectral are approximately given by

$$n_s \approx 1 - \frac{8v_\phi^2}{3\phi_*^2}, \quad (3.24)$$

$$r \approx \frac{64v_\phi^4}{3\phi_*^4}, \quad (3.25)$$

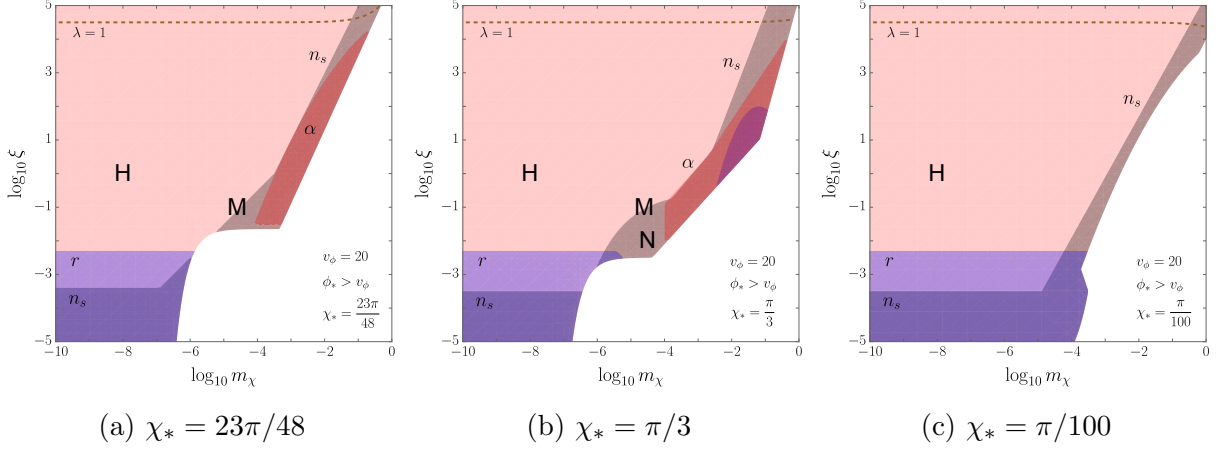


Figure 6: The allowed parameter region in the  $(m_\chi, \xi)$  plane for  $\phi_* > v_\phi = 20$ . For the meanings of the colored regions, see the caption of Figure 5.

$$\alpha \approx -\frac{32v_\phi^4}{9\phi_*^4}. \quad (3.26)$$

The relation between  $\phi_*$  and the e-folding reads

$$N = \frac{(1 + 6\xi)(\phi_*^2 - \phi_e^2) - v_\phi^2 \ln \frac{\phi_*^2}{\phi_e^2} - 6(1 + \xi v_\phi^2) \ln \frac{1 + \xi \phi_*^2}{1 + \xi \phi_e^2}}{8(1 + \xi v_\phi^2)}, \quad (3.27)$$

where we introduce  $\phi_e$  for the final value of  $\phi$ , which can be derived from the SR and ST conditions. From these approximated formulae, we find that the inflation in this case is consistent with the observational data. This is mainly due to the fact that, as in the previous case, a large  $\xi$  results in the flattening of the inflaton potential. In the case of small  $\xi$ , on the other hand, the gradient of the inflaton potential increases, resulting in the inconsistency between theoretical predictions and the observational data, as seen in Figure 6. Since  $\tilde{\beta}$  is approximately given by (3.19) and (3.20) also in this case, we find  $\beta_{\text{iso}}$  sufficiently small. The inflaton behavior discussed here is similar to the previous one with the small VEV  $v_\phi \ll 1$ , since both inflation motions are mainly driven by the radial mode only.

**Large  $m_\chi$  region:** In this case, the inflaton trajectories largely depend on the initial value  $\chi_*$ . For large  $m_\chi$ , we have a significant contribution from the pNGB potential, which in turn allows the inflaton to move in the  $\chi$ -direction. In particular, the natural inflation can be achieved if the initial field values and parameters are tuned, as seen in the middle panel of Figure 6. If both scalar fields drive the inflation, a larger  $\xi$  can lead to the inflation consistent with the observations, as seen in the left and middle panels. A small value of  $\xi$  makes the inflation the chaotic or the natural one, which in any case is excluded by the observational data.

In the large VEV case, we have the upper bound on  $m_\chi$ . For  $\xi \gg 1$ , the power spectrum is approximated as

$$\mathcal{P}_\mathcal{R} \approx \frac{(\lambda\phi_*^2 + 4m_\chi^2 \sin^2 \chi_*)^3 (1 + T_{\mathcal{RS}}^2)}{1536\pi^2 \xi^3 \phi_*^2 m_\chi^4 \sin^2 2\chi_*}. \quad (3.28)$$

A larger  $v_\phi$  requires a larger  $\phi_*$ , which in turn results in a larger  $m_\chi$  due to the Planck normalization  $\mathcal{P}_\mathcal{R}$ . Accordingly, we find that the experimentally allowed parameter value of  $m_\chi$  becomes larger in the present case than that of  $v_\phi \ll 1$  with  $\xi \gg 1$ . On the other hand, for  $\xi \ll 1$ , the power spectrum is approximated as

$$\mathcal{P}_\mathcal{R} \approx \frac{\phi_*^4 (\lambda\phi_*^2 + 4m_\chi^2 \sin^2 \chi_*)^3 (1 + T_{\mathcal{RS}}^2)}{1536\pi^2 [\lambda^2 \phi_*^4 + 4m_\chi^2 (\lambda\phi_*^2 + m_\chi^2) \sin^2 \chi_*]}. \quad (3.29)$$

When  $m_\chi$  is large, namely the pNGB potential is dominant, we have  $\mathcal{P}_\mathcal{R} \propto m_\chi^2$  since the soft-breaking mass parameter is the overall coefficient of the inflaton potential. Therefore, we find that a large  $v_\phi$  leading a large  $\phi_*$  requires a smaller  $m_\chi$  for  $\xi \ll 1$ . This behavior is opposite to the case of  $\xi \gg 1$ .

As for the isocurvature bound, the function  $\tilde{\beta}$  in this case becomes

$$\tilde{\beta} \approx -\frac{2}{\phi^2 \sin^2 \chi} \quad (\xi \ll 1), \quad (3.30)$$

$$\tilde{\beta} \approx -\frac{2\xi}{\sin^2 \chi} \quad (\xi \gg 1), \quad (3.31)$$

for  $m_\chi \gg \sqrt{\lambda}v_\phi$  and  $v_\phi \gg 1$ . We find that  $\beta_{\text{iso}}$  tends to be exponentially small in this type of inflation, similar to the case of  $v_\phi \ll 1$ .

### 3.3.3 $\phi_* < v_\phi$ and $v_\phi = \mathcal{O}(10)$

Let us move on to discussing the different type of inflation with  $\phi_* < v_\phi$ , namely,  $\phi$  rolls down to the vacuum from some smaller field value. As mentioned before, we choose two typical values for the VEV as  $v_\phi = 5$  and 20. We note that the SR inflation is not possible for a small value of VEV, as shown in Eq. (2.28).

We first consider the large VEV case, namely,  $v_\phi = 20$ . Figure 7 shows the allowed parameter region in the  $(m_\chi, \xi)$  plane for  $\phi_* < v_\phi$  and  $N = 55$ . It is noted that a rather small value of  $\xi$  is not excluded because the inflaton potential is sufficiently flat when  $\phi_* < v_\phi$ . On the other hand, the large  $\xi$  region is excluded because the inflaton potential becomes tilted when  $\phi_* < v_\phi$ . These behaviors are in contrast to the previous case with  $\phi_* > v_\phi$ .

**Small  $m_\chi$  region:** When  $m_\chi$  is small, the observables are explicitly written as

$$n_s \approx 1 - \frac{8(1 + \xi v_\phi^2)}{v_\phi^2} - \frac{8(5 + 6\xi v_\phi^2 + \xi^2 v_\phi^4) \phi_*^2}{v_\phi^4}, \quad (3.32)$$

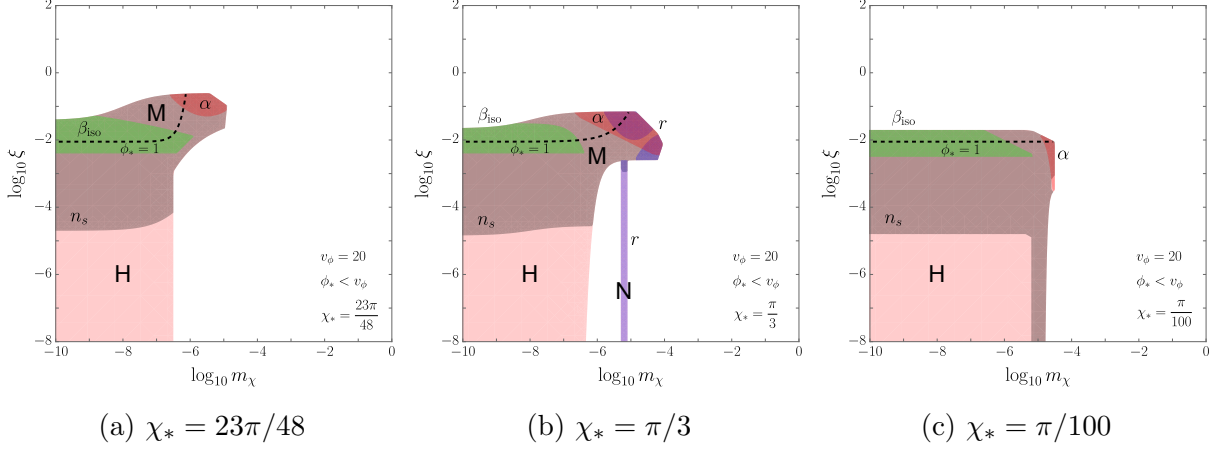


Figure 7: The allowed parameter region in the  $(m_\chi, \xi)$  plane for  $\phi_* < v_\phi = 20$ . The green shaded region is excluded by the isocurvature bound  $\beta_{\text{iso}}$ . The meanings of the other colored regions are same as in Figure 5.

$$r \approx \frac{128(1 + \xi v_\phi^2)^2 \phi_*^2}{v_\phi^4 (1 + \xi \phi_*^2)}, \quad (3.33)$$

$$\alpha \approx -\frac{64(1 + \xi v_\phi^2)^2 (5 + \xi v_\phi^2 - 12\xi^2 v_\phi^2) \phi_*^2}{v_\phi^6}, \quad (3.34)$$

in the region where the SR and ST conditions are satisfied.

If  $\xi \ll 1$ , the observables  $r$  and  $\alpha$  become sufficiently small to be consistent with the observations due to the suppression by a large value of  $v_\phi$ . Furthermore,  $n_s$  is in the experimentally allowed range for  $v_\phi \sim 20$ , as shown in Figure 7. We can say again this behavior is due to the flat inflaton potential in the region  $\phi_* < v_\phi$ .

On the other hand,  $\xi \lesssim \mathcal{O}(1)$  leads to a more tilted inflaton potential in the region  $\phi_* < v_\phi$ . That makes  $n_s$  smaller than the observed value. We find this result from the approximate formula of  $n_s$  in this case,

$$n_s \approx 1 - \frac{8}{v_\phi^2} - 8\xi. \quad (3.35)$$

The severe constraint can be read from this formula and also found in Figure 7. A smaller  $\xi$  is required for the successful inflation under the current conditions.

Finally, we discuss the isocurvature fraction  $\beta_{\text{iso}}$  in this case. The green shaded region in Figure 7 is experimentally excluded by the isocurvature bound. In the region of  $m_\chi \ll v_\phi$ , the function  $\tilde{\beta}$  in (3.18) is approximated as

$$\tilde{\beta} \approx -\frac{8\phi^2}{3v_\phi^4} (1 + \xi v_\phi^2) (3 + 4\xi + 12\xi^2 - 5\xi^2 v_\phi^2 + 12\xi^3 v_\phi^2). \quad (3.36)$$

For sufficiently small or large  $\xi$ ,  $\tilde{\beta}$  is always negative and thus  $\beta_{\text{iso}}$  is found to be small enough. When  $\xi \sim \mathcal{O}(1)$ , on the other hand,  $\tilde{\beta}$  turns out to be positive, which can lead to a large  $\beta_{\text{iso}}$  and is experimentally disfavored. This behavior is actually seen in Figure 7.

**Large  $m_\chi$  region:** In this region, we have three different patterns of inflation, depending on the initial value  $\chi_*$ . In the case where  $\chi_*$  is small, the inflation is mostly driven by  $\phi$ . If  $\chi_*$  is large, both  $\phi$  and  $\chi$  contribute to the inflation, as in the left and middle panels of Figure 7. These two patterns are denoted by the symbols H and M in the figure. As previously discussed, large values of  $\xi$  and  $m_\chi$  lead to a small  $n_s$ . This is due to the fact that the inflaton potential of the radial component is dominated by the quadratic term. Therefore the inflation in which both components join is challenging to achieve in the case of  $\phi_* < v_\phi$  as opposed to the scenario of  $\phi_* > v_\phi$ .

We also have a characteristic behavior in the region with a large  $m_\chi$  and a small  $\xi$  in the middle panel of Figure 7. In this region, the inflation similar to the natural inflation occurs with a very specific value of  $m_\chi$ , as previously discussed in Figure 4. That appears under the conditions that  $\chi_*$  is tuned to realize a fixed value of e-folding  $N$  almost only by the  $\chi$  motion. Consequently,  $r$  becomes larger than the observed value, which is a characteristic feature found from the approximated formula [26]

$$r \approx \frac{32}{\phi_*^2 \sin^2 \chi_*}. \quad (3.37)$$

Since this natural-like inflation is almost driven by a single field  $\chi$ , the hierarchy between  $|1 - n_s|$  and  $|\alpha|$  is hold. We note that in the region where natural-like inflation occurs,  $\tilde{\beta}$  is approximated as

$$\tilde{\beta} \approx -\frac{2}{\phi^2 \sin^2 \chi}, \quad (3.38)$$

which also makes  $\beta_{\text{iso}}$  exponentially small due to its negative value.

### 3.3.4 $\phi_* < v_\phi$ and $v_\phi = \mathcal{O}(1)$

As the final pattern of inflation in the present two-field model, consider the intermediate value of VEV  $\sim \mathcal{O}(1)$ . Figure 8 shows the experimentally allowed parameter region for  $\phi_* < v_\phi = 5$ . One can see that a large portion of area is more severely constrained by the condition  $N = 55$ , compared to the large VEV case of  $\phi_* < v_\phi = 20$ . A large  $\xi$  is not allowed when  $v_\phi$  is small in order to realize a flat inflaton potential. Besides, compared to the large VEV case, the region with a large  $m_\chi$  is also excluded. This is because the inflaton potential is flatter for a larger  $v_\phi$  and a smaller  $m_\chi$ . For large  $m_\chi$  and  $\phi_* < v_\phi$ , the power spectrum is approximated as

$$\mathcal{P}_\mathcal{R} \approx \frac{\lambda^3 v_\phi^{12} (1 + T_{\mathcal{RS}}^2)}{1536 \pi^2 \phi_*^2 [\lambda^2 v_\phi^4 + 4(\lambda v_\phi^2 + m_\chi^2) m_\chi^2 \sin^2 \chi_*]}, \quad (3.39)$$

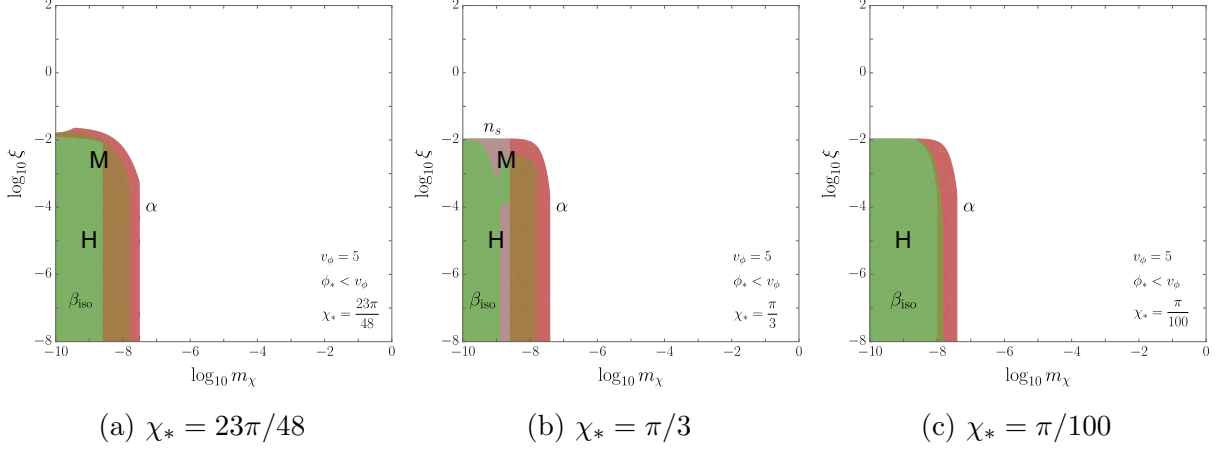


Figure 8: The parameter region in the  $(m_\chi, \xi)$  plane for  $\phi_* < v_\phi = 5$ . The meanings of the colored regions are same as in Figure 7. No experimentally-allowed region is found.

and it is found that a small  $v_\phi$  only allows a small value of  $m_\chi$  because of the Planck normalization.

The parameter region shown in Figure 8, especially in the middle panel, is limited also by the inconsistency with the observed value of  $n_s$ . We find an approximate formula for it as

$$n_s \approx 1 - \frac{8(1 + \xi v_\phi^2)}{v_\phi^2} + \mathcal{O}(m_\chi^2), \quad (3.40)$$

which shows that  $n_s$  gives smaller values than the observation in this case [66]. This is due to the large acceleration of inflaton in this region. The tensor-to-scalar ratio is also approximated as

$$r \approx \frac{128\phi_*^2(1 + \xi v_\phi^2)^2}{v_\phi^4} + \mathcal{O}(m_\chi^2), \quad (3.41)$$

which is still smaller in the entire region where the inflaton potential is flat. The approximated formula for  $\alpha$  is expressed as Eq. (3.34). The current case leads to the conclusion  $\phi_* \ll 1$ , which in turn implies that  $\alpha$  is consistent with the observations provided that  $m_\chi$  is sufficiently small.

Finally, we discuss the isocurvature fraction  $\beta_{\text{iso}}$ . This is found to be large in most entire region in this case. The approximation of  $\tilde{\beta}$  is given by Eq. (3.36). In contrast to the large VEV case, we find  $\tilde{\beta} \approx 0$  at the beginning of inflation. The inflaton is almost insensitive to the  $\phi$ -direction initially, which results in the approximation  $\tilde{\beta} \approx 0$  being realized for a prolonged period during inflation. This means that a relatively small VEV under the condition  $\phi_* < v_\phi$  leads to a large  $\beta_{\text{iso}}$ , which is inconsistent with the observation.

## 4 Cosmic reheating

In this section, we introduce RH neutrinos with Yukawa coupling to the complex scalar field  $\Phi$ , and consider the reheating [67, 68] so that the inflaton heats the thermal bath by the decay to the neutrino sector. In the vacuum after the inflation epoch, the VEV  $v_\phi$  generates the RH neutrino masses and also the pNGB associated with the lepton number  $U(1)_L$  symmetry, called the majoron [69–72]. The majoron has been widely studied in the context of dark matter physics [73–83] and the lepton asymmetry generation [84–88]. In this section, we consider this type of RH neutrino couplings can also be available to the reheating process for non-minimally coupled inflaton.

### 4.1 Coupling to RH neutrinos

We consider the following action for the RH neutrinos  $N_i$  in the Einstein frame,

$$S_N = \int d^4x \sqrt{-g} \left[ \frac{1}{2(1 + 2\xi|\Phi|^2)^{\frac{3}{2}}} \bar{N}_i i \not{D} N_i - \frac{1}{2(1 + 2\xi|\Phi|^2)^2} (f_i \Phi \bar{N}_i P_R N_i + \text{h.c.}) \right], \quad (4.1)$$

where the generation-diagonal Yukawa couplings are introduced between the inflaton and the RH neutrinos, and  $f_i$  are generally complex-valued. The covariant derivative  $\not{D}$  includes the spin connection and  $P_R$  is the chiral projection operator. This form of the action, in particular the  $\Phi$  dependence of the coefficients, can be derived from the original canonical action for  $N_i$  in the Jordan frame and Weyl rescaled with the inflaton field, similarly to the inflaton action in Section 2.1. The action has the lepton number symmetry under which  $N_i$  and  $\Phi$  have the charges +1 and  $-2$ , respectively. This symmetry may correspond to the  $U(1)$  rotation of inflaton field (the origin of pNGB and its soft-breaking mass), which implies a natural support of two-field inflation from a complex scalar. In the following, we focus on the case that  $\phi$  field oscillates at the end of the inflation and decay to the thermal bath through RH neutrinos. We also assume  $\chi$  stays at a constant value  $\bar{\chi}$  during the reheating, and perform the chiral rotation of RH neutrino fields

$$N_i \rightarrow e^{-i\gamma^5(\bar{\chi} + \arg f_i)/2} N_i, \quad (4.2)$$

such that the Yukawa couplings (then the RH neutrino masses) become real valued. During the reheating era, the inflaton oscillates at the bottom of the potential which is determined by the VEV  $u_\phi$ ,

$$u_\phi = \text{Re} \sqrt{\frac{\lambda v_\phi^2 \Omega^2(v_\phi) - m_\chi^2(1 - \cos 2\bar{\chi})}{\lambda \Omega^2(v_\phi) - \xi m_\chi^2(1 - \cos 2\bar{\chi})}}. \quad (4.3)$$

Note that  $u_\phi$  can be vanished if the pNGB potential has a large contribution during the reheating. We expand the scalar field around this VEV so that the scalar field has a canonically normalized kinetic term as

$$\phi = u_\phi + \frac{\Omega^2(u_\phi)}{\sqrt{\Omega^2(u_\phi) + 6\xi^2 u_\phi^2}} \rho, \quad (4.4)$$

and we obtain the action for the scalar fluctuation and the (normalized) RH neutrinos

$$S = \int d^4x \sqrt{-g} \left[ \frac{1}{2} \partial_\mu \rho \partial^\mu \rho - V(\rho) + \frac{1}{2} \bar{N}_i (i \not{D} - m_{N_i}) N_i - \frac{1}{2} y_i \rho \bar{N}_i N_i \right], \quad (4.5)$$

The inflaton coupling to the RH neutrinos  $y_i$  and their mass eigenvalues  $m_{N_i}$  and  $m_\rho$  are given by

$$y_i = \frac{\Omega(u_\phi)}{\sqrt{\Omega^2(u_\phi) + 6\xi^2 u_\phi^2}} \frac{f_i}{\sqrt{2}}, \quad (4.6)$$

$$m_{N_i} = \frac{1}{\Omega(u_\phi)} \frac{f_i}{\sqrt{2}} u_\phi, \quad (4.7)$$

$$m_\rho = \frac{\sqrt{2\lambda\Omega^2(v_\phi) [u_\phi^2(1 + 2\Omega^2(v_\phi)) - v_\phi^2] + m_\chi^2(1 - 5\xi u_\phi^2) \sin^2 \bar{\chi}}}{2\Omega^2(u_\phi) \sqrt{\Omega^2(u_\phi) + 6\xi^2 u_\phi^2}}. \quad (4.8)$$

## 4.2 Reheating and leptogenesis

We examine whether the inflaton coupling to RH neutrinos can be consistent with the reheating of the universe after inflation. A simplified analysis is performed here by taking into account of rough estimations of seesaw-induced neutrino masses and the condition for leptogenesis.

The inflaton decays to the RH neutrino pair,  $\rho \rightarrow N_i N_i$ , during the oscillation. The width is determined by the Yukawa coupling  $y_i$ ,

$$\Gamma_{\rho \rightarrow N_i N_i} = \frac{y_i^2}{16\pi} m_\rho \left( 1 - \frac{4m_{N_i}^2}{m_\rho^2} \right)^{3/2}. \quad (4.9)$$

Once the energy is converted to the  $N_i$  sector, the Standard Model (SM) fields are thermalized by the decay and scattering of  $N_i$  with sufficiently large neutrino Yukawa couplings  $y_{\nu_i}$ . The decay process  $N_i \rightarrow L_j H$ , where  $L_j$  and  $H$  are the leptons and Higgs fields, is effective when  $N_i$  is heavier than the electroweak scale and the decay width is larger than the Hubble parameter at the temperature  $T$ . This condition is roughly given by the present model parameters as

$$T < 21 g_*^{-1/4} y_i v_\phi \left( \frac{m_{\nu_i}}{10^{-1} \text{ eV}} \right)^{1/2} =: T_D, \quad (4.10)$$

where  $g_*$  is the effective degrees of freedom in the radiation with which the temperature is defined. The seesaw-induced light neutrino mass is given by  $m_{\nu_i} = (y_{\nu_i} v_h)^2 / m_{N_i}$  with  $v_h = 175 \text{ GeV}$  (the generation structure is omitted for simplicity of discussion). The scattering of  $N_i$  to the SM sector is also effective if the scattering rate is sufficiently large. This process may be utilized to make the SM sector thermalized radiation component, when the

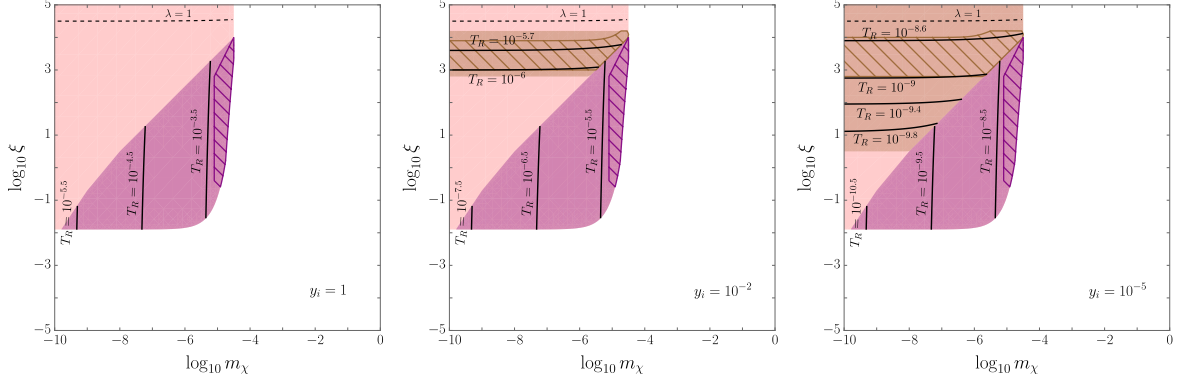


Figure 9: Typical reheating temperature  $T_R$  from the inflaton decay to RH neutrinos with the coupling  $y_i = 1, 10^{-2}, 10^{-5}$ . We show  $T_R$  on the parameter space consistent with the inflationary observables (as an example, Figure 5(b) where the parameters are set to  $v_\phi = 10^{-4}$ ,  $\phi_* > v_\phi$  and  $\chi_* = \pi/3$ ). In the purple (brown) region, the inflaton can decay while oscillating around the origin (the non-trivial vacuum). The decay channel is not open in pink area. We also show the hatched regions where the thermal leptogenesis by RH neutrino decay can work after the reheating is completed ( $T_R > m_{N_i}$ ).

decay process is unavailable in any sense. We roughly evaluate its effectiveness condition by considering the collision term from the scattering, which can be expressed in terms of the present model parameters as

$$T < 0.17 g_*^{-3/2} y_i v_\phi \left( \frac{m_{\nu_i}}{10^{-1} \text{ eV}} \right) =: T_S. \quad (4.11)$$

We have approximated the effective degrees of freedom for the entropy density as equal to that for the energy density. The SM sector is decoupled from the scattering process when its temperature is above  $T_S$ .

As a typical example of this type of reheating, we focus on the parameter region which we have shown, in the middle panel of Figure 5, consistent with the inflationary observable. Figure 9 shows the classification of the reheating and leptogenesis on the allowed region of  $(m_\chi, \xi)$  plane. The uncolored region is excluded by the inflation phenomena only.

The purple regions in Figure 9 correspond to  $u_\phi = 0$ , namely, the inflaton oscillates around the origin. In this case, the decay process may be ineffective if the RH neutrino mass is regarded as small. According to (4.11), the SM sector is thermalized up to the temperature  $T_S$  with  $g_* = 112$ , at which the SM sector decouples from the thermal bath. Since the width (4.9) is large enough, the RH neutrino sector is subsequently heated and reaches the temperature  $T_N$ ,

$$T_N = 0.17 g_*^{-1/4} y_i m_\rho^{1/2}, \quad (4.12)$$

with  $g_* = 5.25$ . Here  $T_N$  is defined by the Hubble time being equal to the width (4.9). (If  $T_N < T_S$ , the  $N_i$  reheating era does not exist and the reheating temperature is given

by  $T_N$ .) As soon as this reheating is over,  $\rho$  is assumed to immediately roll down to the non-trivial vacuum, where the RH neutrinos are massive and the decay process becomes valid for heating the SM sector. If  $T_N < T_D$ , the SM sector is quickly thermalized, and otherwise, the SM thermalization occurs after the universe cools down to  $T_D$ . We then find the final reheating temperature  $T_R$  for the SM sector is given by

$$T_R = \begin{cases} T_N & (T_N < T_S) \\ ((1 - \omega)T_S^3 + \omega T_N^3)^{1/3} & (T_S < T_N < T_D), \\ ((1 - \omega)T_S^3 + \omega T_D^3)^{1/3} & (T_S < T_D < T_N) \end{cases}, \quad (4.13)$$

where  $\omega := g_*^{3N}/(g_*^{\text{SM}} + g_*^{3N})$ . In the region of interest shown in Figure 9, the relation  $T_S < T_N < T_D$  is found to be numerically satisfied everywhere, and the reheating temperature of the radiation then becomes  $T_R \sim 0.36 T_N \sim 0.027 y_i m_\chi^{1/2}$ . These parameter dependence on  $y_i$  and  $m_\chi$  can be seen in the purple regions of Figure 9.

We comment on the leptogenesis, the lepton number generation by the out-of-equilibrium decay of RH neutrinos [89]. The mechanism can work if at least  $T_R > m_{N_i}$  is satisfied. This condition now reads  $0.027 m_\chi^{1/2} > v_\phi$ , which implies  $m_\chi > 1.3 \times 10^{-5}$  for the parameters used in Figure 9. Note that this bound on  $m_\chi$  is independent of the Yukawa couplings and common to three panels in Figure 9. One can see from this bound that only a small portion of the purple region is consistent with successful reheating and leptogenesis in the present inflation scenario.

Another case is that the VEV  $u_\phi$  is non-vanishing, namely, the inflaton oscillates around the non-trivial vacuum. In Figure 9, it corresponds to the colored regions other than purple, where it is numerically checked that the VEV  $u_\phi$  is roughly similar to  $v_\phi$ . In this case, the RH neutrinos  $N_i$  are massive and the reheating by the inflaton decay to  $N_i$  is possible if  $m_\rho > 2m_{N_i}$ . This minimum requirement for reheating imposes the following condition on the model parameters:

$$\Omega^2(v_\phi)\lambda^{1/2} > 2(\Omega^2(v_\phi) + 6\xi^2 v_\phi^2)y_i, \quad (4.14)$$

where we have neglected small  $\bar{\chi}$  contributions. Furthermore, the RH neutrino decay to the SM sector can be sufficiently effective, unlike the  $u_\phi = 0$  case. The reheating by the scattering is subdominant as can be seen by comparing the conditions (4.10) and (4.11), and is not included in the analysis below. The reheating temperature is then given by (4.12) with  $g_* = 112$ , if this temperature is smaller than  $T_D$  and hence the decay process is effective until the universe is heated up to (4.12). That is converted to the constraint on the model parameters as

$$\lambda^{1/2} < 1.5 \times 10^4 v_\phi \sqrt{\Omega^2(v_\phi) + 6\xi^2 v_\phi^2} \left( \frac{m_{\nu_i}}{10^{-1} \text{eV}} \right)^2. \quad (4.15)$$

If not satisfied, the reheating temperature for the SM sector is determined by  $T_D$ , as discussed above. We find the inequality (4.15) generally holds in the present inflation scenario

unless  $v_\phi$  is quite small, and the reheating temperature  $T_R$  is given by (4.12) with  $g_* = 112$ :

$$T_R = 0.052 \frac{\lambda^{1/4} y_i v_\phi^{1/2}}{(\Omega^2(v_\phi) + 6\xi^2 v_\phi^2)^{1/4}} \left( 1 - \frac{4(\Omega^2(v_\phi) + 6\xi^2 v_\phi^2)^2 y_i^2}{\Omega^4(v_\phi) \lambda} \right)^{3/4}, \quad (4.16)$$

where the phase space factor is explicitly included, though it is not so important for evaluating  $T_R$ . As seen from Figure 9, the reheating temperature is not continuously connected to the  $u_\phi = 0$  case. For small  $\xi$ , it scales as  $T_R \propto \xi^{1/2}$  if a rough estimation  $\lambda \propto \xi^2$  from the power spectrum is supposed. On the other hand, for larger  $\xi$  ( $\xi v_\phi \gg 1$ ),  $T_R$  is almost constant and depends linearly on the inflaton coupling  $y_i$  only. The minimum requirement for the reheating (4.14) also leads to a non-trivial upper bound on  $y_i$ . In Figure 9, the pink regions are excluded by this reheating condition. A smaller  $y_i$  is favored that can be read off from the fact that the brown region in Figure 9 becomes wider as  $y_i$  decreases. For a fixed  $y_i$ , (4.14) turns out to give a lower (upper) bound on  $\xi$  for small (large) value of  $\xi$ , if a rough estimation  $\lambda \propto \xi^2$  is taken into account. That indeed corresponds to the horizontal brown bands in the  $(m_\chi, \xi)$  plane.

The thermal leptogenesis is also possible for the  $u_\phi \neq 0$  case. The reheating temperature needs to be at least higher than the (lightest) RH neutrino mass scale, and that implies the parameter bound from (4.7) and (4.16),

$$4y_i^2 < \frac{\lambda \Omega^4(v_\phi)}{(\Omega^2(v_\phi) + 6\xi^2 v_\phi^2)^2} - \frac{50(\Omega^2(v_\phi) \lambda v_\phi)^{2/3}}{\Omega^2(v_\phi) + 6\xi^2 v_\phi^2}. \quad (4.17)$$

This bound is satisfied in the brown hatched regions in Figure 9 where the leptogenesis is available. Assuming  $\lambda$  and  $\xi$  are determined by the inflation phenomena and  $v_\phi$  is a fixed parameter in our analysis, (4.17) gives an upper bound on the inflaton Yukawa coupling  $y_i$ . This is the phase space bound of the inflaton decay and does not strongly affect the model parameter constraints once the decay channel is open. These behaviors can be seen from the  $y_i$  difference in Figure 9. Note that (4.17) (the brown hatched region) is necessarily stronger than (4.14) (the brown region) since the latter is the vanishing limit of the phase space. For a fixed  $y_i$ , (4.17) gives the bound on  $\xi$ , almost independently of  $m_\chi$ . Taking a rough relation  $\lambda \propto \xi^2$  obtained from the power spectrum in mind, a lower (upper) bound on  $\xi$  for small (large) value of  $\xi$  can be derived from (4.17), which corresponds to the horizontal brown-hatched bands in the  $(m_\chi, \xi)$  plane.

We finally comment on several other possibilities of reheating in the present inflation model. In the pink region of Figure 9, the inflaton decay to heavy  $N_i$  is forbidden and the main decay mode to the SM sector would be a top quark pair. The reheating only with this mode gives a roughly estimated temperature  $T_R \sim 10^{-14} \lambda^{1/4} v_\phi^{1/2} (m_{\nu_i}/\text{eV})^2$ , which is suppressed by large  $N_i$  masses and becomes around  $\mathcal{O}(\text{MeV})$  to  $\mathcal{O}(\text{GeV})$  for the parameters in the pink regions. This temperature is just before the big bang nucleosynthesis, but would need to be improved, e.g., for the leptogenesis being successful. As another possibility, the inflaton can also interact with the scalar sector through the Higgs portal coupling, inflaton

potential terms, etc. While we do not consider this type of reheating process in this paper, it would be interesting to examine it in connection with the inflaton shift to the non-trivial vacuum, and will be left for future work.

## 5 Conclusions

In this paper, we study the two-field inflation originated from one complex scalar field with a non-vanishing VEV and a non-minimal coupling to gravity. We introduce the  $\mu$  parameter to characterize the multi-field nature and classify the inflaton trajectories in the field space to three typical types, depending on which field components contribute to the inflationary expansion. According to this classification, there are several cases that only the radial component contributes to the inflation, only the pNGB mode contributes, and both do. The parameter  $\mu$  tends to be large when both modes contribute to the inflation.

Furthermore, we make the detailed classifications on the VEV, the soft-breaking mass  $m_\chi$ , and the initial value of the inflaton field  $\phi_*$  and  $\chi_*$ , as the classification covers the above three typical patterns. For each classification, we show the parameter space consistent with the current cosmological observations. It is found that the experimental results favor the inflation mainly driven by the radial component of the scalar field, but we also find other parameter space consistent with the observations for these three types of inflationary expansion.

While the natural inflation is known to generally require that the VEV is larger than the Planck scale, we show that VEVs smaller than the Planck scale allow the successful inflation with a sufficient contribution from pNGB modes under the condition  $\phi_* > v_\phi$  and  $\xi \lesssim 1$ . Moreover, we find that even when VEV is rather small, the inflation is also successful for large  $m_\chi$  and  $\chi_*$  where the contribution from the pNGB mode is comparable to the radial mode. For a VEV larger than the Planck scale, the pNGB-contributed inflation is possible without fine tuning. On the other hand, the small field inflation with  $\phi_* < v_\phi$  is shown to generally contradict with the observations unless sufficient contribution of the radial component exists. It is also found that a tiny value of VEV is not favored for  $\phi_* < v_\phi$  even when the pNGB mode contributes to some extent.

We also examine whether the reheating by the inflaton decay to the RH neutrinos is possible where the complex scalar field generating the Majorana mass term plays the roll of inflaton. The VEV at the end of the inflation can be away from the scalar potential vacuum due to non-trivial field value which is a result of the inflation. Taking this into the account and evaluating the reheating temperature, we show that the parameter region with large  $m_\chi$  is allowed in addition to the region with moderately large  $\xi$ . This is because the inflaton oscillates around the origin in the region where  $m_\chi$  is sufficiently large. We would need detailed numerical analysis to examine the consistency with successful leptogenesis, but that is beyond the scope of this paper. Some mechanism to move the background  $\chi$

field is also a left future problem so that the non-trivial potential vacuum is realized after the inflation dynamics and reheating.

## Acknowledgments

The work of Y.A. is supported by JSPS Overseas Research Fellowships. The work of K.Y. is supported by JSPS KAKENHI Grant No. JP20K03949.

## A Scalar field dynamics

In this appendix, we summarize the details of the scalar sector.

### A.1 EOMs

The general form of the action for the scalar fields  $\varphi^a$  is

$$S = \int d^4x \sqrt{-g} \left[ -\frac{R}{2} + \frac{1}{2} K_{ab}(\varphi) \partial_\mu \varphi^a \partial^\mu \varphi^b - V(\varphi) \right]. \quad (\text{A.1})$$

From this, the general EOM of the scalar field reads

$$\nabla^2 \varphi^a + \gamma_{bc}^a(\varphi) \partial_\mu \varphi^b \partial^\mu \varphi^c + K^{ab}(\varphi) \partial_b V(\varphi) = 0, \quad (\text{A.2})$$

where  $\nabla$  is the covariant derivative evaluated by the Einstein frame metric  $g_{\mu\nu}$ . The Levi-Civita connection in the scalar field geometry is given by

$$\gamma_{bc}^a = \frac{1}{2} K^{ad} (\partial_b K_{dc} + \partial_c K_{bd} - \partial_d K_{bc}). \quad (\text{A.3})$$

We assume

$$ds^2 = g_{\mu\nu} dx^\mu dx^\nu = dt^2 - a(t)^2 d\vec{x}^2, \quad (\text{A.4})$$

and  $\varphi^a$  depends only on the time. Then the EOM reduces to

$$\ddot{\varphi}^a + 3H\dot{\varphi}^a + \gamma_{bc}^a \dot{\varphi}^b \dot{\varphi}^c + K^{ab} \partial_b V = 0, \quad (\text{A.5})$$

where the dot is the derivative with respect to  $t$ , and the Hubble parameter is defined as  $H := \dot{a}/a$ . When we introduce the e-folding  $N$  by  $dN = H dt$ , the EOMs (A.5) become

$$\frac{d^2 \varphi^a}{dN^2} + \gamma_{bc}^a \frac{d\varphi^b}{dN} \frac{d\varphi^c}{dN} + (3 - \varepsilon) \left( \frac{d\varphi^a}{dN} + K^{ab} \partial_b \ln V \right) = 0. \quad (\text{A.6})$$

In this derivation, we have used the Friedmann equation

$$H^2 = \frac{1}{3} \left( \frac{1}{2} K_{ab} \dot{\varphi}^a \dot{\varphi}^b + V(\varphi) \right), \quad \dot{H} = -\frac{1}{2} K_{ab} \dot{\varphi}^a \dot{\varphi}^b, \quad (\text{A.7})$$

and introduced the slow-roll parameter  $\varepsilon$  given by

$$\varepsilon := -\frac{\dot{H}}{H^2} = \frac{1}{2} K_{ab} \frac{d\varphi^a}{dN} \frac{d\varphi^b}{dN}. \quad (\text{A.8})$$

## A.2 Geometry of scalar fields

We consider the complex scalar  $\Phi = \phi e^{i\chi}/\sqrt{2}$  with the non-minimal coupling  $\xi$ . The metric of the scalar field space is found to be

$$K_{ab} = \text{diag} \left( \frac{1 + \xi\phi^2 + 6\xi^2\phi^2}{(1 + \xi\phi^2)^2}, \frac{\phi^2}{1 + \xi\phi^2} \right). \quad (\text{A.9})$$

The non-vanishing Levi-Civita connection in this space is given by

$$\gamma_{11}^1 = -\frac{\xi\phi(1 - 6\xi + \xi\phi^2 + 6\xi^2\phi^2)}{(1 + \xi\phi^2)(1 + \xi\phi^2 + 6\xi^2\phi^2)}, \quad (\text{A.10})$$

$$\gamma_{22}^1 = -\frac{\phi}{1 + \xi\phi^2 + 6\xi^2\phi^2}, \quad (\text{A.11})$$

$$\gamma_{12}^2 = \gamma_{21}^2 = \frac{1}{\phi(1 + \xi\phi^2)}. \quad (\text{A.12})$$

Here the index 1 and 2 correspond to  $\phi$  and  $\chi$ , respectively. The Ricci scalar of this geometry becomes

$$\mathcal{R} = \frac{4\xi(1 + 3\xi + \xi\phi^2 + 6\xi^2\phi^2)}{(1 + \xi\phi^2 + 6\xi^2\phi^2)^2}. \quad (\text{A.13})$$

We note  $\mathcal{R} \rightarrow 0$  as the non-minimal coupling  $\xi \rightarrow 0$ .

## B Slow-roll and slow-turn parameters

In the space of field  $\varphi^a$ , the velocity is given by its derivative with respect to the e-folding, i.e.,  $d\varphi^a/dN$ , and the (covariant) acceleration of the field vector is  $\eta^a = d^2\varphi^a/dN^2 + \gamma_{bc}^a(d\varphi^c/dN)(d\varphi^b/dN)$ . The slow-roll and slow-turn parameters are defined by the (half) size of the velocity vector and the parallel and vertical components of the acceleration vector as [46]:

$$\varepsilon = \frac{1}{2} K_{ab} \frac{d\varphi^a}{dN} \frac{d\varphi^b}{dN}, \quad (\text{B.1})$$

$$\frac{\eta_{\parallel}^a}{v} = \frac{1}{v} K_{ab} \hat{e}_{\parallel}^a \left( \frac{d^2\varphi^b}{dN^2} + \gamma_{dc}^b \frac{d\varphi^c}{dN} \frac{d\varphi^d}{dN} \right), \quad (\text{B.2})$$

$$\frac{\eta_{\perp}^a}{v} = \frac{1}{v} K_{ab} \hat{e}_{\perp}^a \left( \frac{d^2\varphi^b}{dN^2} + \gamma_{dc}^b \frac{d\varphi^c}{dN} \frac{d\varphi^d}{dN} \right). \quad (\text{B.3})$$

For the acceleration vector, dividing by the speed  $v$  implies to express the rate of the change of the field velocity. When the slow-roll and slow-turn approximation are satisfied,  $\varepsilon, |\eta_{\parallel}|/v, \eta_{\perp}/v \ll 1$ , these parameters can be explicitly written by the inflaton potential and the field space metric, as given in (2.19)–(2.21).

We here present the slow-roll and slow-turn parameters in our two-field inflation model, especially in the approximation used in the text.

When the soft-breaking mass  $m_\chi$  is sufficiently large, the inflation is mainly driven by the  $\chi$  potential, and the slow-roll parameters are given by

$$\varepsilon \approx \frac{2}{\phi^2} \left[ \frac{(1 - \xi\phi^2)^2}{1 + \xi\phi^2 + 6\xi^2\phi^2} + (1 + \xi\phi^2) \cot^2 \chi \right], \quad (\text{B.4})$$

$$\begin{aligned} \frac{\eta_{\parallel}}{v} \approx & \frac{1 + \xi\phi^2}{\phi^2} \left[ \frac{2(1 - \xi\phi^2)^2(1 + 3\xi\phi^2 + 12\xi^2\phi^2) \tan^2 \chi}{(1 + \xi\phi^2 + 6\xi^2\phi^2)^2} \right. \\ & + \csc^2 \chi [1 + 5\xi\phi^2 + 12\xi^2\phi^2 + 2\xi^2\phi^4 + 12\xi^3\phi^4 + (1 - \xi\phi^2) \cos 2\chi] \\ & \left. + 4(1 - \xi\phi^2) \right] \Big/ \left[ (1 - \xi\phi^2)^2 \tan^2 \chi + (1 + \xi\phi^2)(1 + \xi\phi^2 + 6\xi^2\phi^2) \right]. \end{aligned} \quad (\text{B.5})$$

Both parameters do not depend on  $m_\chi$  since the inflaton  $\chi$  potential is proportional to it.

When  $\phi$  takes a larger value than  $v_\phi$  during the inflation, the slow-roll parameters are expressed as

$$\varepsilon \approx \frac{8}{\lambda^2 \xi (1 + 6\xi) \phi^4} \left[ [\lambda(1 + \xi v_\phi^2) - 2\xi m_\chi^2 \sin^2 \chi]^2 + m_\chi^4 \xi^2 (1 + 6\xi) \sin^2 2\chi \right], \quad (\text{B.6})$$

$$\begin{aligned} \frac{\eta_{\parallel}}{v} \approx & \frac{8\xi}{\lambda\phi^2} \left[ \frac{[\lambda(1 + \xi v_\phi^2) - 2\xi m_\chi^2 \sin^2 \chi]^3}{\xi^2 (1 + 6\xi)^2} + \frac{2[\lambda(1 + \xi v_\phi^2) - 2\xi m_\chi^2 \sin^2 \chi] m_\chi^4 \sin^2 2\chi}{1 + 6\xi} \right. \\ & \left. - \xi m_\chi^6 \cos 2\chi \sin^2 2\chi \right] \Big/ \left[ \frac{[\lambda(1 + \xi v_\phi^2) - 2\xi m_\chi^2 \sin^2 \chi]^2}{\xi(1 + 6\xi)} + \xi m_\chi^4 \sin^2 2\chi \right], \end{aligned} \quad (\text{B.7})$$

On the other hand, in the small field region with  $\phi < v_\phi$ , the slow-roll parameters become

$$\varepsilon \approx \frac{8\phi^2}{\lambda^2 v_\phi^8} \left[ [\lambda v_\phi^2 (1 + \xi v_\phi^2) - 2m_\chi^2 \sin^2 \chi]^2 + m_\chi^4 \sin^2 2\chi \right], \quad (\text{B.8})$$

$$\begin{aligned} \frac{\eta_{\parallel}}{v} \approx & \frac{4}{\lambda v_\phi^4} \left[ [\lambda v_\phi^2 (1 + \xi v_\phi^2) - 2m_\chi^2 \sin^2 \chi]^3 + 3[\lambda v_\phi^2 (1 + \xi v_\phi^2) - 2m_\chi^2 \sin^2 \chi] m_\chi^4 \sin^2 2\chi \right. \\ & \left. - 2m_\chi^6 \cos 2\chi \sin^2 2\chi \right] \Big/ \left[ [\lambda v_\phi^2 (1 + \xi v_\phi^2) - 2m_\chi^2 \sin^2 \chi]^2 + m_\chi^4 \sin^2 2\chi \right]. \end{aligned} \quad (\text{B.9})$$

## C Formulae of cosmological observables

### C.1 Transfer functions

In the multi-field inflation, the isocurvature mode turn into the curvature fluctuations, thus, it is important to represent the expression for the transport functions describing the super-horizon evolution of the perturbation, according to Ref. [46]. The effective mass matrix is defined as

$$M^a_b := K^{ac} (\partial_c \partial_b \ln V - \gamma_{cb}^d \partial_d \ln V) + \frac{1}{3} \varepsilon \mathcal{R} \hat{e}_\perp^a K_{bc} \hat{e}_\perp^c. \quad (\text{C.1})$$

With the expression of the basis vector (2.23) and the Ricci scalar in the field space (A.13) at hand, the matrix  $M$  is fully determined by the couplings and background field values in the present inflation model. With this matrix, the transfer functions are defined as

$$T_{SS} = \exp \left[ \int_{N_*}^N dN' (K_{ac} \hat{e}_{\parallel}^c M^a_b \hat{e}_{\parallel}^b - K_{ac} \hat{e}_{\perp}^c M^a_b \hat{e}_{\perp}^b) \right], \quad (\text{C.2})$$

$$T_{RS} = \int_{N_*}^N dN' \frac{\eta_{\perp}}{v} \exp \left[ \int_{N_*}^{N'} dN'' (K_{ac} \hat{e}_{\parallel}^c M^a_b \hat{e}_{\parallel}^b - K_{ac} \hat{e}_{\perp}^c M^a_b \hat{e}_{\perp}^b) \right]. \quad (\text{C.3})$$

These are also the functions of model parameters and field values through the expressions of the basis vectors and the slow-roll parameter (2.21). Note that the transfer functions (C.2) and (C.3) always take positive values.

## C.2 Cosmological observables

Here we give the exact form of the cosmological observables. First, the power spectrum and the tensor-to-scalar ratio are given as the following explicit forms in our model,

$$\mathcal{P}_{\mathcal{R}} = \frac{(1 + \xi \phi_*^2)^4 (1 + T_{RS}^2) V(\phi_*, \chi_*)^3}{3\pi^2 \phi_*^2} \left/ \left[ \frac{[\lambda(1 + \xi v_{\phi}^2)(\phi_*^2 - v_{\phi}^2) + 2m_{\chi}^2(1 - \xi \phi_*^2) \sin^2 \chi_*]^2}{1 + \xi \phi_*^2 + 6\xi^2 \phi_*^2} + m_{\chi}^4(1 + \xi \phi_*^2) \sin^2 2\chi_* \right] \right., \quad (\text{C.4})$$

$$r = \frac{2\phi_*^2}{(1 + \xi \phi_*^2)^4 (1 + T_{RS}^2) V(\phi_*, \chi_*)^2} \times \left[ \frac{[\lambda(1 + \xi v_{\phi}^2)(\phi_*^2 - v_{\phi}^2) + 2m_{\chi}^2(1 - \xi \phi_*^2) \sin^2 \chi_*]^2}{1 + \xi \phi_*^2 + 6\xi^2 \phi_*^2} + m_{\chi}^4(1 + \xi \phi_*^2) \sin^2 2\chi_* \right]. \quad (\text{C.5})$$

The power spectrum consisting of the correlation function of scalar fluctuations depends on the positive power of  $T_{RS}$ . On the other hand,  $r$ , which consists of the ratio of tensor fluctuations to scalar ones, depends on the inverse power of  $T_{RS}$ . The spectral index  $n_s$  and its running  $\alpha$  are also written by the field values in the present model under the slow-roll and slow-turn approximation [46],

$$n_s = 1 - 2\varepsilon_* + 2K_{ab*} \hat{e}_{N*}^a M^b_{c*} \hat{e}_{N*}^c, \quad (\text{C.6})$$

$$\alpha = [-K^{ab} \partial_a \ln V \partial_b (-2\varepsilon + 2K_{cd} \hat{e}_N^c M^d_e \hat{e}_N^e)]_*, \quad (\text{C.7})$$

where

$$\hat{e}_N = \frac{1}{\sqrt{1 + T_{RS}^2}} \hat{e}_{\parallel} + \frac{T_{RS}}{\sqrt{1 + T_{RS}^2}} \hat{e}_{\perp}. \quad (\text{C.8})$$

The isocurvature fraction is determined by the transfer functions as

$$\beta_{\text{iso}} = \frac{T_{SS}^2}{1 + T_{RS}^2 + T_{SS}^2}. \quad (\text{C.9})$$

Using the explicit expressions of the basis vectors (2.22), (2.23) and the transfer functions (C.2), (C.3) defined by using the matrix (C.1), all these cosmological observables can also be expressed by the parameters and field values in the present inflation model. In the text, various approximations of these formulae are presented, depending on the magnitude of coupling constants and field values.

## References

- [1] A. A. Starobinsky, *A New Type of Isotropic Cosmological Models Without Singularity*, *Phys. Lett. B* **91** (1980) 99–102.
- [2] A. H. Guth, *The Inflationary Universe: A Possible Solution to the Horizon and Flatness Problems*, *Phys. Rev. D* **23** (1981) 347–356.
- [3] A. D. Linde, *A New Inflationary Universe Scenario: A Possible Solution of the Horizon, Flatness, Homogeneity, Isotropy and Primordial Monopole Problems*, *Phys. Lett. B* **108** (1982) 389–393.
- [4] A. Albrecht and P. J. Steinhardt, *Cosmology for Grand Unified Theories with Radiatively Induced Symmetry Breaking*, *Phys. Rev. Lett.* **48** (1982) 1220–1223.
- [5] A. A. Starobinsky, *Dynamics of Phase Transition in the New Inflationary Universe Scenario and Generation of Perturbations*, *Phys. Lett. B* **117** (1982) 175–178.
- [6] A. D. Linde, *Chaotic Inflation*, *Phys. Lett. B* **129** (1983) 177–181.
- [7] M. Berg, E. Pajer, and S. Sjors, *Dante’s Inferno*, *Phys. Rev. D* **81** (2010) 103535, [0912.1341 \[hep-th\]](#).
- [8] J. McDonald, *Sub-Planckian Two-Field Inflation Consistent with the Lyth Bound*, *JCAP* **09** (2014) 027, [1404.4620 \[hep-ph\]](#).
- [9] G. Barenboim and W.-I. Park, *Spiral Inflation*, *Phys. Lett. B* **741** (2015) 252–255, [1412.2724 \[hep-ph\]](#).
- [10] A. Achúcarro, V. Atal, and Y. Welling, *On the viability of  $m^2\phi^2$  and natural inflation*, *JCAP* **07** (2015) 008, [1503.07486 \[astro-ph.CO\]](#).
- [11] G. G. Ross, G. German, and J. A. Vazquez, *Hybrid Natural Inflation*, *JHEP* **05** (2016) 010, [1601.03221 \[astro-ph.CO\]](#).
- [12] E. McDonough, A. H. Guth, and D. I. Kaiser, *Nonminimal Couplings and the Forgotten Field of Axion Inflation*, [2010.04179 \[hep-th\]](#).
- [13] K. Deshpande, S. Kumar, and R. Sundrum, *TwInflation*, *JHEP* **07** (2021) 147, [2101.06275 \[hep-ph\]](#).
- [14] J.-O. Gong and K. S. Jeong, *Axion-driven hybrid inflation over a barrier*, *Phys. Rev. D* **104** no. 4, (2021) 043511, [2101.11173 \[hep-ph\]](#).
- [15] H. M. Lee and A. G. Menkara, *Pseudo-Nambu-Goldstone inflation with twin waterfalls*, *Phys. Lett. B* **834** (2022) 137483, [2206.05523 \[hep-ph\]](#).
- [16] N. U. Khan, N. Ijaz, and M. U. Rehman, *New inflation in the waterfall region*, *Phys. Rev. D* **108** no. 12, (2023) 123545, [2309.06953 \[hep-ph\]](#).
- [17] D. Baumann and L. McAllister, *Inflation and String Theory*. Cambridge Monographs on Mathematical Physics. Cambridge University Press, 5, 2015. [1404.2601 \[hep-th\]](#).
- [18] M. Cicoli, J. P. Conlon, A. Maharana, S. Parameswaran, F. Quevedo, and I. Zavala, *String cosmology: From the early universe to today*, *Phys. Rept.* **1059** (2024) 1–155, [2303.04819 \[hep-th\]](#).

- [19] K. Freese, J. A. Frieman, and A. V. Olinto, *Natural inflation with pseudo - Nambu-Goldstone bosons*, *Phys. Rev. Lett.* **65** (1990) 3233–3236.
- [20] F. C. Adams, J. R. Bond, K. Freese, J. A. Frieman, and A. V. Olinto, *Natural inflation: Particle physics models, power law spectra for large scale structure, and constraints from COBE*, *Phys. Rev. D* **47** (1993) 426–455, [hep-ph/9207245](#).
- [21] C. Savage, K. Freese, and W. H. Kinney, *Natural Inflation: Status after WMAP 3-year data*, *Phys. Rev. D* **74** (2006) 123511, [hep-ph/0609144](#).
- [22] N. K. Stein and W. H. Kinney, *Natural inflation after Planck 2018*, *JCAP* **01** no. 01, (2022) 022, [2106.02089](#) [[astro-ph.CO](#)].
- [23] A. Salvio, *Natural-scalaron inflation*, *JCAP* **10** (2021) 011, [2107.03389](#) [[hep-ph](#)].
- [24] A. Mukuno and J. Soda, *Chromo-natural warm inflation*, [2402.08849](#) [[hep-th](#)].
- [25] F. L. Bezrukov and M. Shaposhnikov, *The Standard Model Higgs boson as the inflaton*, *Phys. Lett. B* **659** (2008) 703–706, [0710.3755](#) [[hep-th](#)].
- [26] J. Rubio, *Higgs inflation*, *Front. Astron. Space Sci.* **5** (2019) 50, [1807.02376](#) [[hep-ph](#)].
- [27] V.-M. Enckell, K. Enqvist, S. Rasanen, and L.-P. Wahlman, *Higgs- $R^2$  inflation - full slow-roll study at tree-level*, *JCAP* **01** (2020) 041, [1812.08754](#) [[astro-ph.CO](#)].
- [28] A. S. Koshelev and A. Tokareva, *Non-local self-healing of Higgs inflation*, *Phys. Rev. D* **102** (2020) 123518, [2006.06641](#) [[hep-th](#)].
- [29] P. Pareek and A. Nautiyal, *Non-canonical Higgs inflation*, *Class. Quant. Grav.* **41** no. 3, (2024) 035003, [2306.01576](#) [[astro-ph.CO](#)].
- [30] C. Gross, O. Lebedev, and T. Toma, *Cancellation Mechanism for Dark-Matter-Nucleon Interaction*, *Phys. Rev. Lett.* **119** no. 19, (2017) 191801, [1708.02253](#) [[hep-ph](#)].
- [31] Y. Abe, T. Toma, and K. Tsumura, *Pseudo-Nambu-Goldstone dark matter from gauged  $U(1)_{B-L}$  symmetry*, *JHEP* **05** (2020) 057, [2001.03954](#) [[hep-ph](#)].
- [32] N. Okada, D. Raut, and Q. Shafi, *Pseudo-Goldstone dark matter in a gauged  $B - L$  extended standard model*, *Phys. Rev. D* **103** no. 5, (2021) 055024, [2001.05910](#) [[hep-ph](#)].
- [33] Y. Abe, T. Toma, K. Tsumura, and N. Yamatsu, *Pseudo-Nambu-Goldstone dark matter model inspired by grand unification*, *Phys. Rev. D* **104** no. 3, (2021) 035011, [2104.13523](#) [[hep-ph](#)].
- [34] N. Okada, D. Raut, Q. Shafi, and A. Thapa, *Pseudo-Goldstone dark matter in  $SO(10)$* , *Phys. Rev. D* **104** no. 9, (2021) 095002, [2105.03419](#) [[hep-ph](#)].
- [35] T. Abe and Y. Hamada, *A model of pseudo-Nambu-Goldstone dark matter from a softly broken  $SU(2)$  global symmetry with a  $U(1)$  gauge symmetry*, *PTEP* **2023** no. 3, (2023) 033B04, [2205.11919](#) [[hep-ph](#)].
- [36] D.-Y. Liu, C. Cai, X.-M. Jiang, Z.-H. Yu, and H.-H. Zhang, *Ultraviolet completion of pseudo-Nambu-Goldstone dark matter with a hidden  $U(1)$  gauge symmetry*, *JHEP* **02** (2023) 104, [2208.06653](#) [[hep-ph](#)].
- [37] T. Hirai and K.-i. Maeda, *Gauge invariant cosmological perturbations in generalized Einstein theories*, *Astrophys. J.* **431** (1994) 6–19, [astro-ph/9404023](#).

- [38] D. I. Kaiser, *Primordial spectral indices from generalized Einstein theories*, *Phys. Rev. D* **52** (1995) 4295–4306, [astro-ph/9408044](#).
- [39] D. I. Kaiser, *Conformal Transformations with Multiple Scalar Fields*, *Phys. Rev. D* **81** (2010) 084044, [1003.1159 \[gr-qc\]](#).
- [40] H. Abedi and A. M. Abbassi, *Gravitational constant in multiple field gravity*, *JCAP* **05** (2015) 026, [1411.4854 \[gr-qc\]](#).
- [41] M. Sasaki and T. Tanaka, *Superhorizon scale dynamics of multiscalar inflation*, *Prog. Theor. Phys.* **99** (1998) 763–782, [gr-qc/9801017](#).
- [42] S. Groot Nibbelink and B. J. W. van Tent, *Density perturbations arising from multiple field slow roll inflation*, [hep-ph/0011325](#).
- [43] S. Groot Nibbelink and B. J. W. van Tent, *Scalar perturbations during multiple field slow-roll inflation*, *Class. Quant. Grav.* **19** (2002) 613–640, [hep-ph/0107272](#).
- [44] D. Seery and J. E. Lidsey, *Primordial non-Gaussianities from multiple-field inflation*, *JCAP* **09** (2005) 011, [astro-ph/0506056](#).
- [45] D. Langlois and S. Renaux-Petel, *Perturbations in generalized multi-field inflation*, *JCAP* **04** (2008) 017, [0801.1085 \[hep-th\]](#).
- [46] C. M. Peterson and M. Tegmark, *Testing Two-Field Inflation*, *Phys. Rev. D* **83** (2011) 023522, [1005.4056 \[astro-ph.CO\]](#).
- [47] J.-O. Gong, *Multi-field inflation and cosmological perturbations*, *Int. J. Mod. Phys. D* **26** no. 01, (2016) 1740003, [1606.06971 \[gr-qc\]](#).
- [48] P. Christodoulidis, D. Roest, and E. I. Sfakianakis, *Angular inflation in multi-field  $\alpha$ -attractors*, *JCAP* **11** (2019) 002, [1803.09841 \[hep-th\]](#).
- [49] C. Gordon, D. Wands, B. A. Bassett, and R. Maartens, *Adiabatic and entropy perturbations from inflation*, *Phys. Rev. D* **63** (2000) 023506, [astro-ph/0009131](#).
- [50] J. M. Bardeen, *Gauge Invariant Cosmological Perturbations*, *Phys. Rev. D* **22** (1980) 1882–1905.
- [51] H. Kodama and M. Sasaki, *Cosmological Perturbation Theory*, *Prog. Theor. Phys. Suppl.* **78** (1984) 1–166.
- [52] D. H. Lyth, *Large Scale Energy Density Perturbations and Inflation*, *Phys. Rev. D* **31** (1985) 1792–1798.
- [53] M. Sasaki, *Large Scale Quantum Fluctuations in the Inflationary Universe*, *Prog. Theor. Phys.* **76** (1986) 1036.
- [54] V. F. Mukhanov, H. A. Feldman, and R. H. Brandenberger, *Theory of cosmological perturbations. Part 1. Classical perturbations. Part 2. Quantum theory of perturbations. Part 3. Extensions*, *Phys. Rept.* **215** (1992) 203–333.
- [55] D. Wands, N. Bartolo, S. Matarrese, and A. Riotto, *An Observational test of two-field inflation*, *Phys. Rev. D* **66** (2002) 043520, [astro-ph/0205253](#).

- [56] L. Amendola, C. Gordon, D. Wands, and M. Sasaki, *Correlated perturbations from inflation and the cosmic microwave background*, *Phys. Rev. Lett.* **88** (2002) 211302, [astro-ph/0107089](#).
- [57] S. Karamitsos and A. Pilaftsis, *Frame Covariant Nonminimal Multifield Inflation*, *Nucl. Phys. B* **927** (2018) 219–254, [1706.07011 \[hep-ph\]](#).
- [58] F. Di Marco, F. Finelli, and R. Brandenberger, *Adiabatic and isocurvature perturbations for multifield generalized Einstein models*, *Phys. Rev. D* **67** (2003) 063512, [astro-ph/0211276](#).
- [59] M. Beltran, J. Garcia-Bellido, J. Lesgourgues, and M. Viel, *Squeezing the window on isocurvature modes with the lyman-alpha forest*, *Phys. Rev. D* **72** (2005) 103515, [astro-ph/0509209](#).
- [60] J. Hamann, S. Hannestad, G. G. Raffelt, and Y. Y. Y. Wong, *Isocurvature forecast in the anthropic axion window*, *JCAP* **06** (2009) 022, [0904.0647 \[hep-ph\]](#).
- [61] M. Sasaki and E. D. Stewart, *A General analytic formula for the spectral index of the density perturbations produced during inflation*, *Prog. Theor. Phys.* **95** (1996) 71–78, [astro-ph/9507001](#).
- [62] **Planck** Collaboration, Y. Akrami *et al.*, *Planck 2018 results. X. Constraints on inflation*, *Astron. Astrophys.* **641** (2020) A10, [1807.06211 \[astro-ph.CO\]](#).
- [63] D. L. Lorenzoni, D. I. Kaiser, and E. McDonough, *Natural Inflation with Exponentially Small Tensor-To-Scalar Ratio*, [2405.13881 \[astro-ph.CO\]](#).
- [64] Y. Abe, T. Toma, and K. Yoshioka, *Non-thermal Production of PNCB Dark Matter and Inflation*, *JHEP* **03** (2021) 130, [2012.10286 \[hep-ph\]](#).
- [65] C. van de Bruck and C. Longden, *Running of the Running and Entropy Perturbations During Inflation*, *Phys. Rev. D* **94** no. 2, (2016) 021301, [1606.02176 \[astro-ph.CO\]](#).
- [66] G. Barenboim, E. J. Chun, and H. M. Lee, *Coleman-Weinberg Inflation in light of Planck*, *Phys. Lett. B* **730** (2014) 81–88, [1309.1695 \[hep-ph\]](#).
- [67] L. F. Abbott, E. Farhi, and M. B. Wise, *Particle Production in the New Inflationary Cosmology*, *Phys. Lett. B* **117** (1982) 29.
- [68] E. W. Kolb, *The Early Universe*, vol. 69. Taylor and Francis, 5, 2019.
- [69] Y. Chikashige, R. N. Mohapatra, and R. D. Peccei, *Are There Real Goldstone Bosons Associated with Broken Lepton Number?*, *Phys. Lett. B* **98** (1981) 265–268.
- [70] J. Schechter and J. W. F. Valle, *Neutrino Decay and Spontaneous Violation of Lepton Number*, *Phys. Rev. D* **25** (1982) 774.
- [71] G. B. Gelmini and M. Roncadelli, *Left-Handed Neutrino Mass Scale and Spontaneously Broken Lepton Number*, *Phys. Lett. B* **99** (1981) 411–415.
- [72] I. Z. Rothstein, K. S. Babu, and D. Seckel, *Planck scale symmetry breaking and majoron physics*, *Nucl. Phys. B* **403** (1993) 725–748, [hep-ph/9301213](#).
- [73] V. Berezhinsky and J. W. F. Valle, *The KeV majoron as a dark matter particle*, *Phys. Lett. B* **318** (1993) 360–366, [hep-ph/9309214](#).

- [74] S. Matsumoto and K. Yoshioka, *Deep Correlation Between Cosmic-Ray Anomaly and Neutrino Masses*, *Phys. Rev. D* **82** (2010) 053009, 1006.1688 [[hep-ph](#)].
- [75] M. Frigerio, T. Hambye, and E. Masso, *Sub-GeV dark matter as pseudo-Goldstone from the seesaw scale*, *Phys. Rev. X* **1** (2011) 021026, 1107.4564 [[hep-ph](#)].
- [76] F. S. Queiroz and K. Sinha, *The Poker Face of the Majoron Dark Matter Model: LUX to keV Line*, *Phys. Lett. B* **735** (2014) 69–74, 1404.1400 [[hep-ph](#)].
- [77] C. Garcia-Cely and J. Heeck, *Neutrino Lines from Majoron Dark Matter*, *JHEP* **05** (2017) 102, 1701.07209 [[hep-ph](#)].
- [78] T. Brune and H. Päs, *Massive Majorons and constraints on the Majoron-neutrino coupling*, *Phys. Rev. D* **99** no. 9, (2019) 096005, 1808.08158 [[hep-ph](#)].
- [79] Y. Abe, Y. Hamada, T. Ohata, K. Suzuki, and K. Yoshioka, *TeV-scale Majorogenesis*, *JHEP* **07** no. 07, (2020) 105, 2004.00599 [[hep-ph](#)].
- [80] S. K. Manna and A. Sil, *Majorons revisited: Light dark matter as a FIMP*, *Phys. Rev. D* **108** no. 7, (2023) 075026, 2212.08404 [[hep-ph](#)].
- [81] C. Biggio, L. Calibbi, T. Ota, and S. Zanchini, *Majoron dark matter from a type II seesaw model*, *Phys. Rev. D* **108** no. 11, (2023) 115003, 2304.12527 [[hep-ph](#)].
- [82] K. Akita and M. Niibo, *Updated constraints and future prospects on majoron dark matter*, *JHEP* **07** (2023) 132, 2304.04430 [[hep-ph](#)].
- [83] C. Bonilla, A. E. Carcamo Hernandez, B. Saez Diaz, S. Kovalenko, and J. Marchant Gonzalez, *Dark matter from a radiative inverse seesaw majoron model*, *Phys. Lett. B* **847** (2023) 138282, 2306.08453 [[hep-ph](#)].
- [84] A. Pilaftsis, *Electroweak Resonant Leptogenesis in the Singlet Majoron Model*, *Phys. Rev. D* **78** (2008) 013008, 0805.1677 [[hep-ph](#)].
- [85] M. Le Dall and A. Ritz, *Leptogenesis and the Higgs Portal*, *Phys. Rev. D* **90** no. 9, (2014) 096002, 1408.2498 [[hep-ph](#)].
- [86] T. Alanne, T. Hugle, M. Platscher, and K. Schmitz, *Low-scale leptogenesis assisted by a real scalar singlet*, *JCAP* **03** (2019) 037, 1812.04421 [[hep-ph](#)].
- [87] Y. Abe, T. Ito, and K. Yoshioka, *Leptonic CP asymmetry and Light flavored scalar*, *JHEP* **01** (2023) 019, 2110.11096 [[hep-ph](#)].
- [88] D. M. Barreiros, H. B. Câmara, R. G. Felipe, and F. R. Joaquim, *Scalar-singlet assisted leptogenesis with CP violation from the vacuum*, *JHEP* **01** (2023) 010, 2211.00042 [[hep-ph](#)].
- [89] M. Fukugita and T. Yanagida, *Baryogenesis Without Grand Unification*, *Phys. Lett. B* **174** (1986) 45–47.